



# Thermal history and extensional exhumation of a high-temperature crystalline complex (Hirkadağ Massif, Central Anatolia)



Côme Lefebvre<sup>a,b,\*</sup>, M. Kalijn Peters<sup>a</sup>, Philip C. Wehrens<sup>c</sup>, Fraukje M. Brouwer<sup>d</sup>, Herman L.M. van Roermund<sup>a</sup>

<sup>a</sup> Department of Earth Sciences, Utrecht University, 3508 TA Utrecht, The Netherlands

<sup>b</sup> Department of Earth Sciences, University of Minnesota, Minneapolis, MN 55455, USA

<sup>c</sup> Institute of Geological Sciences, University of Bern, CH-3012 Bern, Switzerland

<sup>d</sup> Faculty of Earth and Life Sciences (FALW), VU University, 1081 HV Amsterdam, The Netherlands

## ARTICLE INFO

### Article history:

Received 27 March 2015

Accepted 25 September 2015

Available online 9 October 2015

### Keywords:

High temperature metamorphism

P–T–t–d evolution

Exhumation tectonics

Central Anatolia

## ABSTRACT

The Central Anatolian Crystalline Complex (CACC) is a large continental domain exposed in central Turkey that was affected by high temperature metamorphism during the Late Cretaceous. As a result of this event, Paleozoic sediments became metamorphosed, initially under Barrovian conditions, then overprinted locally by high temperature–low pressure metamorphism, and intruded by widespread batholiths. In this study we focus on the crystalline Hirkadağ Massif located in the central part of the CACC, where we applied an integrated approach involving metamorphic, structural and geochronological analysis in order to elucidate its tectonic history from burial to exhumation. Our metamorphic study reveals that conditions of metamorphism reached ~7–8 kbar/700 °C and were relatively homogeneous at the scale of the Hirkadağ Massif. Coeval with the regional metamorphism, the rocks were intensely deformed as reflected by isoclinal folding, the development of a pervasive foliation and top-to-the-SE shearing. This was followed by decompression to pressures of ~3–4 kbar at 800 °C, which may be linked to the emplacement of local granodioritic intrusions at ~77 Ma. Subsequent cooling of the Hirkadağ high-grade metamorphic and intrusive rocks is indicated by <sup>40</sup>Ar/<sup>39</sup>Ar cooling ages of  $68.8 \pm 0.9$  Ma (biotite) and  $67.0 \pm 1.2$  Ma (potassium feldspar). Evidence for tectonic exhumation has been identified within the marbles at the NE margin of the Hirkadağ Massif, in the form of discrete protomylonitic and mylonitic shear bands showing a consistent N40–60 top-to-NE sense of shear. Further east, the contact between brecciated mylonitic marbles and non-metamorphic conglomerates preserves the typical structural features of an upper-crustal detachment fault. Restoration of the Hirkadağ Massif and the CACC to their late Cretaceous configuration suggests that the LP–HT metamorphism, magmatism and extensional structures evolved as a result of the development and exhumation of a ~N–S trending magmatic arc experiencing regional E–W extension above an active subduction zone.

Published by Elsevier B.V.

## 1. Introduction

Low pressure-high temperature (LP–HT) metamorphic rocks exposed in orogenic belts offer a good opportunity to investigate crustal processes associated with syn-convergence exhumation of crystalline domains. Such domains of LP–HT metamorphism, commonly characterized by the occurrence of high-grade metamorphic rocks associated with magmatic intrusions, evolve in tectonic settings involving an anomalously high geothermal gradient. In order to identify possible processes explaining the resulting high temperatures at shallow-crustal levels and subsequent exhumation of these rocks, integrated

studies on natural examples that preserved such elevated thermal conditions are required. The Central Anatolian Crystalline Complex (CACC), located within the Turkish segment of the Alpine orogenic belt, provides a natural laboratory where an extensive crystalline domain was affected by regional high temperature metamorphism during the Late Cretaceous (Fig. 1a) (Ketin, 1966; Göncüoğlu, 1977). This HT event, which lasted for ~20 Myr (from ~95 to 75 Ma) caused upper amphibolite/granulite regional metamorphism (grading into greenschist facies at higher structural levels) of a sequence of Paleozoic–Mesozoic platform sediments (Erkan, 1976; Seymen, 1981). Following peak metamorphism, ubiquitous granitic, monzonitic and syenitic plutons intruded at upper crustal levels (Akıman et al., 1993), while remains of coeval sub-aerial volcanism are locally preserved. The Gülşehir–Avanos area (Fig. 2) exposes two exhumed metamorphic/intrusive massifs, separated by a well-preserved sedimentary basin that contains Upper Cretaceous volcanics (Köksal and Göncüoğlu, 1997; Whitney and

\* Corresponding author at: Department of Earth Sciences, University of Minnesota, Minneapolis, MN 55455, USA.

E-mail address: [lefebvre@umn.edu](mailto:lefebvre@umn.edu) (C. Lefebvre).

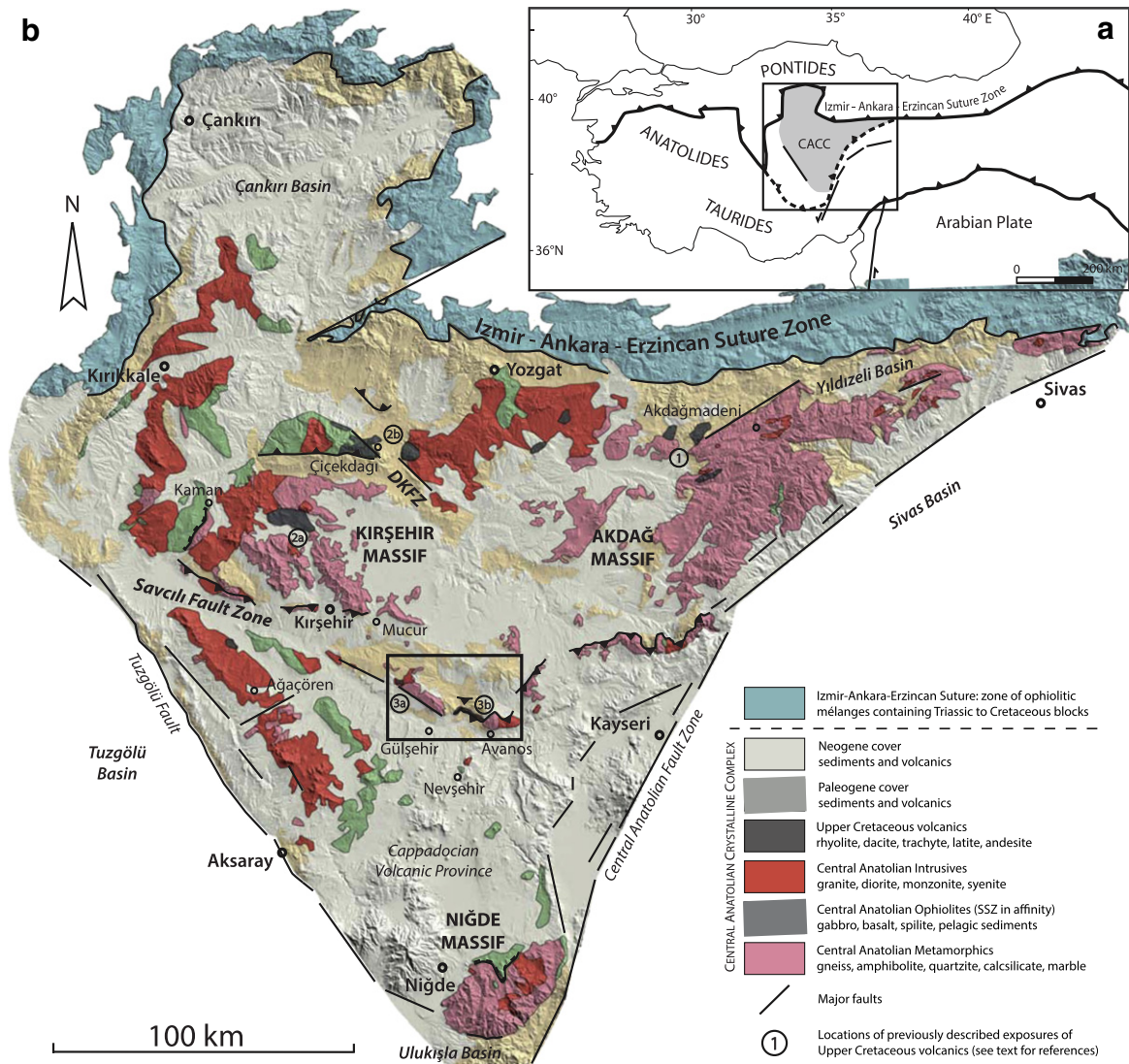


**Fig. 1.** a) Simplified tectonic outline of Turkey, b) simplified geological map of the Central Anatolian Crystalline Complex (CACC) draped onto a shaded relief image prepared from digital elevation model. Circled numbers show the locations of previously described exposures of Upper Cretaceous volcanics (see text for corresponding references). Rectangle indicates the Güleşhir–Avanos area presented in Fig. 2.

Dilek, 2001). The region thus presents an excellent opportunity to investigate the evolution of an exhuming crustal HT complex at depth, and its relationship with the coeval sub-aerial processes occurring at and near the Earth's surface.

We present a detailed geological study of the HT Hırkadağ Massif, located in the center of the CACC. We complemented and extended existing petrographical work performed on the high grade metasediments (Whitney and Dilek, 2001) with whole-rock and mineral chemical analyses, mineral equilibria calculations and thermodynamic modeling, in order to estimate their P–T conditions and trajectories. In addition, we present a detailed structural map of the entire Hırkadağ Massif, focusing on the tectonic evolution from pervasive ductile shearing at peak metamorphic conditions to localized brittle tectonics near the contact with the adjacent sedimentary basin. We integrate our results with titanite U/Pb and biotite and K-feldspar  $^{40}\text{Ar}/^{39}\text{Ar}$  thermochronology on a granodioritic intrusion and a metapelite of the Hırkadağ Massif (reported in Lefebvre, 2011), which provide time-constraints on the cooling history of the Hırkadağ HT complex through its crustal journey toward the Earth surface. Finally, based on our new results we discuss the role of LP-HT metamorphism together with mechanisms of exhumation of the HT crystalline rocks at the scale of the CACC and plate tectonics.

## 2. Geological setting

Turkey consists of a segment of the EW trending Alpine–Himalayan orogenic belt (Fig. 1) and is composed of a complex amalgamation of continental and oceanic fragments. In the north, the Paleozoic and Mesozoic sequences of the Pontides were affected by the Hercynian and Cimmeride orogenies (Şengör and Yilmaz, 1981). The Pontides are bounded in the south by the Izmir–Ankara–Erzincan suture zone (IAESZ), demarcating the position of the northern branch of the Neotethys (Okay and Tüysüz, 1999). South of the suture, the Anatolide and Tauride belts of Gondwana affinity represent south-derived micro-continental fragments that collided with Eurasia in late Cretaceous to Eocene times (Görür et al., 1984; Kaymakci et al., 2009; Meijers et al., 2010). The two largest metamorphic massifs of the Anatolides comprise the Menderes Massif in the west and the Central Anatolian Crystalline Complex (CACC) in the central part of Turkey (Fig. 1).

### 2.1. Central Anatolian Crystalline Complex (CACC)

The CACC (Göncüoğlu et al., 1991), which is also known as Kırşehir Block (Görür et al., 1984), is located immediately south of the central



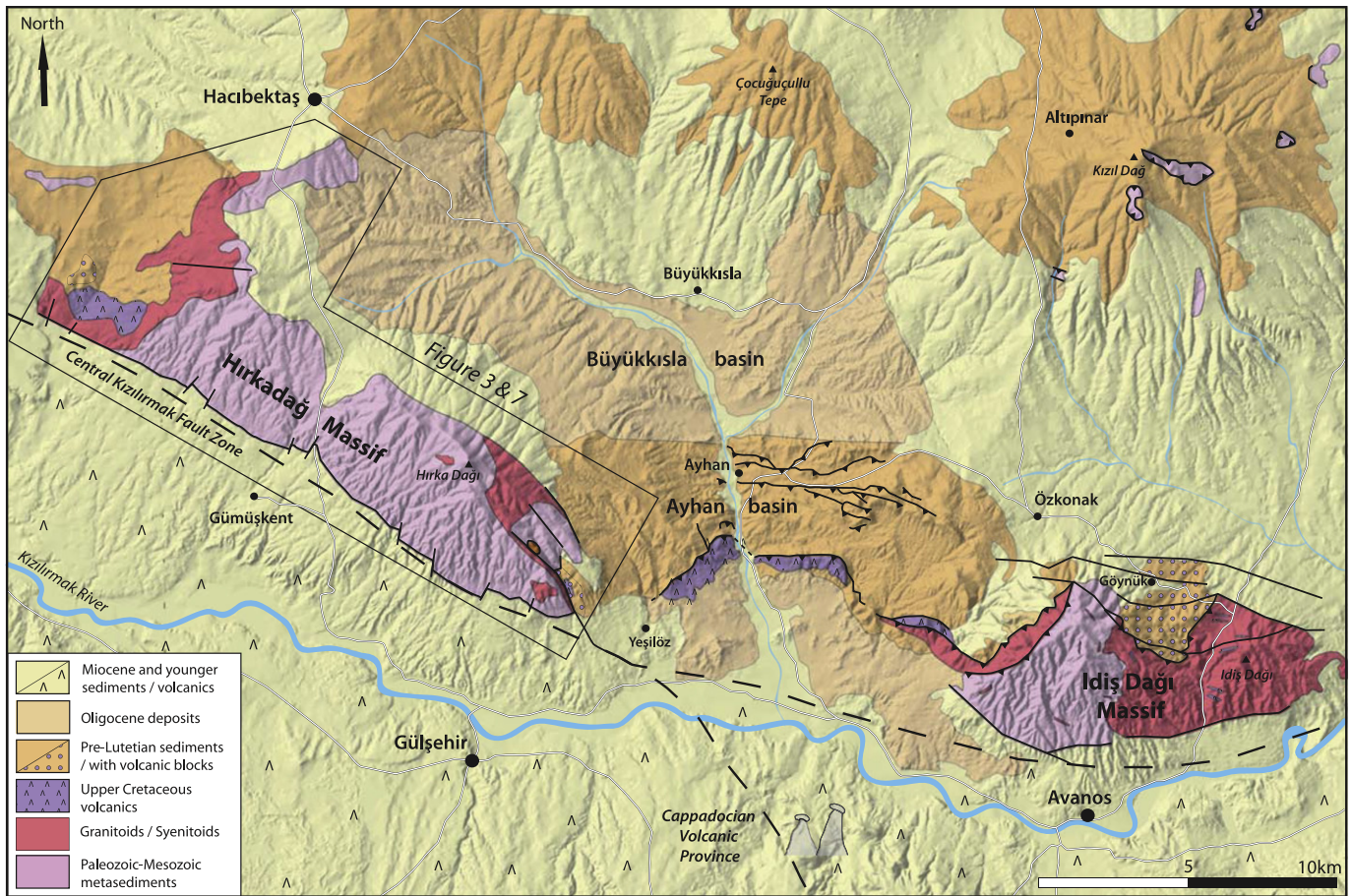


Fig. 2. Simplified geological and tectonic map of the Gölşehir–Avanos area based on Atabay (1989), Köksal and Göncüoğlu (1997), Advokaat et al. (2014) and Lefebvre (2015).

segment of the Izmir–Ankara–Erzincan suture zone, and is defined as a large continental domain dominated by crystalline rocks, including metasediments (central Anatolian Metamorphics, CAM), ophiolitic remnants (central Anatolian Ophiolites, CAO) and magmatic intrusions. In the west and the east, it is separated from the Anatolide and Tauride belts by two major intra-continental transcurrent faults: the Tuzgözü Fault and the Central Anatolian Fault Zone, respectively. The CAM are the oldest rocks in the region, consisting of metamorphosed Paleozoic–Mesozoic sequences comprising clastic rocks and platform carbonates (Göncüoğlu, 1977; Göncüoğlu et al., 1991). The CAM are geographically distributed over three sub-massifs: 1) the Akdağ Massif in the north-east (Vache, 1963), 2) the Niğde Massif in the south (Göncüoğlu, 1977) and the 3) Kırşehir Massif in the north-west (Seymen, 1981) (Fig. 1b). In the Kırşehir Massif, a regional metamorphic field gradient has been identified ranging from upper amphibolite/granulite facies to greenschist facies over a horizontal distance of ~50 km (Erkan, 1976; Seymen, 1981). Thermobarometric estimates of peak metamorphic conditions of high-grade schists range from 700 to 800 °C at 6–8 kbar, with locally a re-heating overprint at lower pressures (2–4 kbar) (Kocak and Leake, 1994; Whitney and Dilek, 1998; Whitney et al., 2001). The timing of regional metamorphism is constrained by ~91–84 Ma U/Pb ages of monazite and zircon (Whitney et al., 2003; Whitney and Hamilton, 2004). Few remnants of oceanic crust, tectonically emplaced on top of the CAM, witness late Cretaceous obduction. These klippen of oceanic material, defined as the CAO, show the typical geochemical features of Supra-Subduction-Zone Ophiolites (Göncüoğlu and Türel, 1993; Yaliniz and Göncüoğlu, 1998; Yaliniz, 2008). Soon after obduction widespread magmatism, mostly seen in the western part of the CACC, formed elongated felsic, mafic and intermediate plutons intruding through both the CAM and

CAO (Fig. 1b) (Erler and Göncüoğlu, 1996). This magmatic event, which lasted for ~20 Ma (from ~95 until 75 Ma), comprises a large range of compositions varying from granitic, granodioritic, gabbroic, monzonitic to syenitic, with calc-alkaline to alkaline affinity (Akıman et al., 1993; Boztuğ et al., 2007). There is no consensus about the tectonic setting in which the Central Anatolian magmatism evolved, as geochemical discrimination diagrams suggest volcanic arc, within-plate, and syn- to post-collisional origins for the formation of the granitoids (Göncüoğlu and Türel, 1994; Kadioğlu et al., 2003; İlbeli et al., 2004).

In two localities evidence has been provided that exhumation of the HT rocks was associated with extensional detachments between a high-grade metasedimentary footwall and a non-metamorphic ophiolite hanging wall, i.e., in the Niğde Massif (Whitney and Dilek, 1997; Gautier et al., 2002; Umhoefer et al., 2007) and near Kaman in the Kırşehir Massif (Lefebvre et al., 2011, 2012). In addition, discrete ductile shear zones affecting granitoids near Yozgat and Ağaçören indicate that at least some of the intrusives were emplaced syntectonically during an extension phase (Isik et al., 2008; Isik, 2009). The timing of unroofing of the high grade metamorphic and intrusive rocks is constrained by apatite fission track ages (AFT) from the intrusive suites generally indicating an early to middle Paleocene (57–62 Ma) cooling below ~100 °C (Boztuğ and Jonckheere, 2007) although a few younger AFT ages have also been reported in the region (Fayon et al., 2001; Umhoefer et al., 2007).

The sub-aerial counterpart of the late Cretaceous intrusions is represented by remnants of Upper Cretaceous felsic to intermediate volcanics preserved in three main areas: (1) The Saraykent volcanics (labeled as 1 in Fig. 1b) (Kuşcu and Floyd, 1995; Gençalioglu-Kuşcu and Floyd, 2002); (2) the Karahıdır and Kötüdağ volcanics c (labeled as 2a and 2b in Fig. 1b) (Seymen, 1982); (3) In the Gölşehir–Avanos area near

Gümüşkent, the Kızıltepe volcanics (labeled as 3a in Fig. 1b) (Aydın, 1985), and the “Karahıdır” volcanics in the east (labeled 3b in Fig. 1b) (Köksal and Göncüoğlu, 1997; Köksal et al., 2001). A new  $^{40}\text{Ar}/^{39}\text{Ar}$  plagioclase analysis from a “Karahıdır” andesite gives an age of  $72.1 \pm 1.5$  Ma (Advokaat et al., 2014).

Recent paleomagnetic data by Lefebvre et al. (2013) demonstrated that the CACC consists of three tectonic blocks that rotated and converged relative to each other during its collision with the Pontides. The block rotations were accommodated along two main fault zones. In the north, the postulated Delice–Kozaklı Fault Zone (DKFZ) is a NW–SE trending right-lateral transpressional corridor (Lefebvre et al., 2013), along which the Çiçekdağı basin recorded syn-depositional N–S shortening during late Eocene (~39–35 Ma) (Gülyüz et al., 2013) (Fig. 1). In the south, the Savcılı Fault Zone (SFZ) is a 150 km long ESE–WNW trending and NNE-vergent thrust belt across the CACC, active after Middle Eocene times (Fig. 1) (e.g. Oktay, 1981; Seymen, 1984; Köksal and Göncüoğlu, 1997). Recent Rb–Sr and Ar–Ar dating on SFZ gouge illites indicates at least two phases of active faulting at ~40 Ma and ~23 Ma (Isik et al., 2014).

## 2.2. The Gülşehir–Avanos area

The Gülşehir–Avanos area (Fig. 2) is located in the center of the CACC, at the northern boundary of the Central Anatolian Volcanic Province of Cappadocia. It contains two crystalline massifs, the Hırkadağ Massif in the west and İdiş Dağı Massif in the east, separated by the Ayhan basin.

The two crystalline massifs are isolated from the major central Anatolian metamorphic massifs by two fault zones (the SFZ in the north and the Central Kızılırmak Fault Zone in the south) and Paleogene to Neogene basins (Figs. 1 and 2). The metamorphic rocks of the Hırkadağ Massif comprise a metasedimentary succession similar to the one described from the north-westerly Kırşehir and southerly Niğde massifs (Seymen, 1981; Aydın, 1985; Atabey et al., 1987; Teklehaïmanot, 1993). In the east, the İdiş Dağı metamorphic rocks consist of massive marbles with amphibolite intercalations that represent the uppermost unit of the CAM. They are intruded by alkali-feldspar and quartz syenites, which were geochemically classified as post-collisional A-type igneous rocks and are believed to have intruded later than the granitoids in the Gülşehir–Avanos area (Fig. 2) (Göncüoğlu et al., 1993; Köksal and Göncüoğlu, 1997). The northern border of the İdiş Dağı Massif is thrustured northwards over the Ayhan basin fill (Köksal and Göncüoğlu, 1997). Also referred to as the Özkonak zone, the Ayhan basin is described as a fold and thrust belt with Eocene turbidites and conglomerates displaying overturned and recumbent folds as well as E–W trending reverse and north-vergent thrust faults (Genç and Yürür, 2010; Advokaat et al., 2014). In the south, its basal unit contains conglomerate with intercalated andesitic volcanics ( $72.1 \pm 1.5$  Ma) and syn-sedimentary normal faults suggesting that it was an extensional basin from the onset of sedimentation (Fig. 2) (Advokaat et al., 2014). The Ayhan basin is currently separated from the Hırkadağ Massif by active high-angle normal faults, but syn-sedimentary deformation and intra-basinal unconformities, as well as the absence of metamorphic or granitic debris in the lower part of the stratigraphy (Member Y2 of the Yeşilöz Formation (Advokaat et al., 2014) corresponding to the Göynük Olistostrome (Köksal and Göncüoğlu, 1997), Elmadere Olistostrome (Teklehaïmanot, 1993) and Saytepe Member of Atabey (1989), (Fig. 3)), indicate that these faults were mainly active during infilling of the Ayhan basin. The rest of the Ayhan basin is unconformably covered by post-Lutetian red beds of the Büyükkışla basin and younger deposits (Advokaat et al., 2014; Lefebvre, 2015). Advokaat et al. (2014) proposed that the Büyükkışla basin was affected by S-vergent contraction involving thrusting and folding resulting to ~17–27 km of shortening; however, none of the claimed evidences accounting for this tectonic scenario can be confirmed in the field (Lefebvre, 2015).

## 2.3. The Hırkadağ Massif

The Hırkadağ Massif is a NW–SE trending, 4 km wide belt, which is topographically higher than the surrounding areas (Fig. 3). Historically, the Hırkadağ Massif has been separately studied in domains exposed west and east of the Kırşehir–Nevşehir road (Aydın, 1985; Teklehaïmanot, 1993). In this study, we have compiled and investigated both the western and eastern parts of the Hırkadağ Massif, and traced the boundaries of the metamorphic units initially recognized in the east (Teklehaïmanot, 1993) toward the west (Fig. 3). Three lithological units were identified in the metamorphic rocks of the Hırkadağ Massif. From bottom to top and from south to north, they include (1) a lower unit characterized by alternating muscovite-bearing quartzite beds and garnet and sillimanite-bearing schists, as well as amphibolites, calc-silicates and banded marbles. Individual quartzite beds may be up to ten meters thick, and the quartzite-schist sequence is up to several hundred meters thick; (2) an intermediate unit dominated by calc-silicate rocks with variable silica and calcium contents, interbedded with meter-scale marble, amphibolite and quartzite layers. Quartzites are associated with metapelitic schists. Pegmatite and aplitic granites with cm-scale feldspar crystals are present; and (3) an upper unit characterized by massive marbles and minor calc-silicate rocks. The marbles are coarse to fine-grained, and do not present any compositional banding, in contrast to those found in the lowermost unit.

The western and easternmost parts of the Hırkadağ Massif are intruded by a network of felsic dykes and veins. The Akçataş Granitoids in the western part of the Hırkadağ Massif are mainly composed of granite, granodiorite, quartz diorite, monzonite and syenite, which crystallized at shallow depth (Aydın, 1985). The Hırkadağ intrusives are mainly composed of coarse K-feldspar, plagioclase and quartz, do not contain any trace of ductile fabrics and show clear cross-cutting relationships with the foliated country-rocks.

Previous estimates of peak metamorphic conditions on metapelitic schists from the southern margin of the Hırkadağ Massif indicated 670–830 °C at 4–6 kbar based on mineral assemblages and metamorphic reactions (Teklehaïmanot, 1993). Geothermo-barometric analyses of similar metapelites yielded conditions of 670–710 °C and ~7 kbar, overprinted by LP–HT metamorphism (3 kbar; >650 °C) (Whitney and Dilek, 2001). The proposed metamorphic grade thus ranges from upper amphibolite/granulite facies along the SW margin to greenschist facies along the NE margin, although no thermobarometric calculations were obtained from the NE rocks (Whitney and Dilek, 2001) and the decrease of metamorphic grade is based on correlation to structural level through the massif (Teklehaïmanot, 1993). The ductile deformation history of the metasediments is complicated. The rocks show a pervasive ductile foliation affected by several folding phases, cross-cut by C-type shear band cleavages, with brittle high-angle normal faults bounding the metamorphic rocks in the east and the south. (Teklehaïmanot, 1993; Whitney and Dilek, 2001)

In its present state, the Hırkadağ Massif appears to be an uplifted horst, with the Central Kızılırmak Fault Zone (Fig. 3) running along its SW margin (Teklehaïmanot, 1993; Toprak, 1994). The occurrence of horizontally overlying Quaternary travertine along this fault zone and connected fault branches suggests recent tectonic activity (Toprak, 1994). Along the NE margin, the Upper Miocene–Pliocene Yüksekli Formation, composed of tuffaceous gravel, sand, sandstone and conglomerate, unconformably overlies the Hırkadağ Massif (Atabey, 1989). A normal fault contact relationship is reported in the south (Teklehaïmanot, 1993). Due to poor exposure of the westernmost granitoids of the Hırkadağ Massif, the nature of the contact with pre-Eocene volcanics and conglomerates still remains unknown.

The eastern part of the Hırkadağ Massif is separated from the Göynük/Elmadere and Saytepe Formations by a tectonic contact (Fig. 3). This contact, exposed in the Gürleğen valley, has previously been considered as a flat-lying thrust bringing the crystalline rocks eastward on top of the Göynük/Elmadere Formation (Teklehaïmanot,



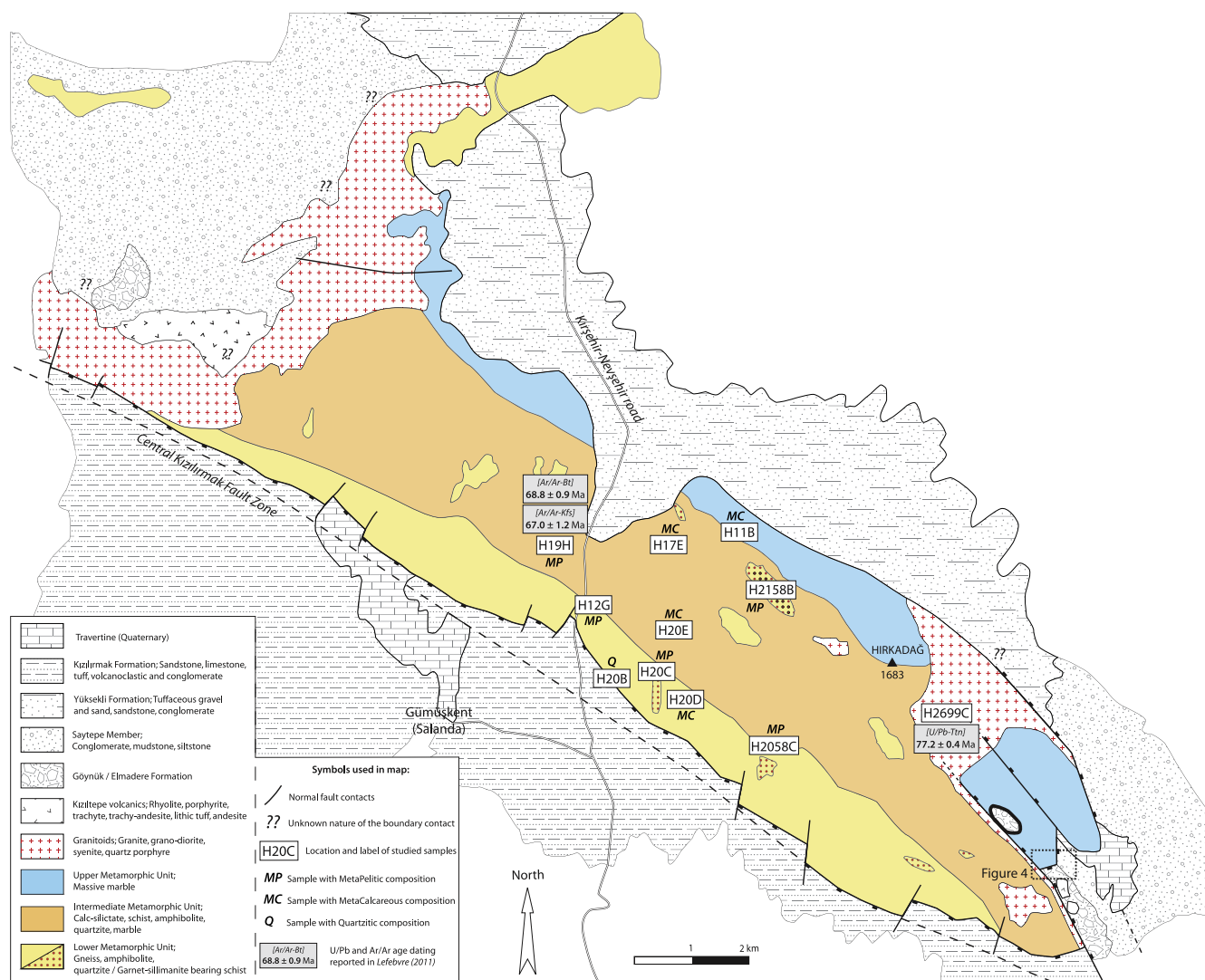


**Fig. 3.** Detailed geological map of the Hırkadağ Massif (in color) and surrounding sedimentary and volcanic cover (in black and white), with location and composition of the samples used for petrological study and geochronology from Lefebvre (2011).

1993). Although the nature of the contact is difficult to determine (Whitney and Dilek, 2001), the presence of crystalline rocks in a lower structural position with respect to the Göynük/Elmadere Formation and the occurrence of flat-lying travertine deposits along the valley are in good agreement with a geometry of a high-angle normal

fault (Fig. 4). This contact may have shared activity with branches of the Kızılirmak Fault to the SE, but structural and stratigraphic analysis of the Ayhan basin has shown that most of the displacement along this fault took place prior to the Lutetian (Middle Eocene) (Advokaat et al., 2014).

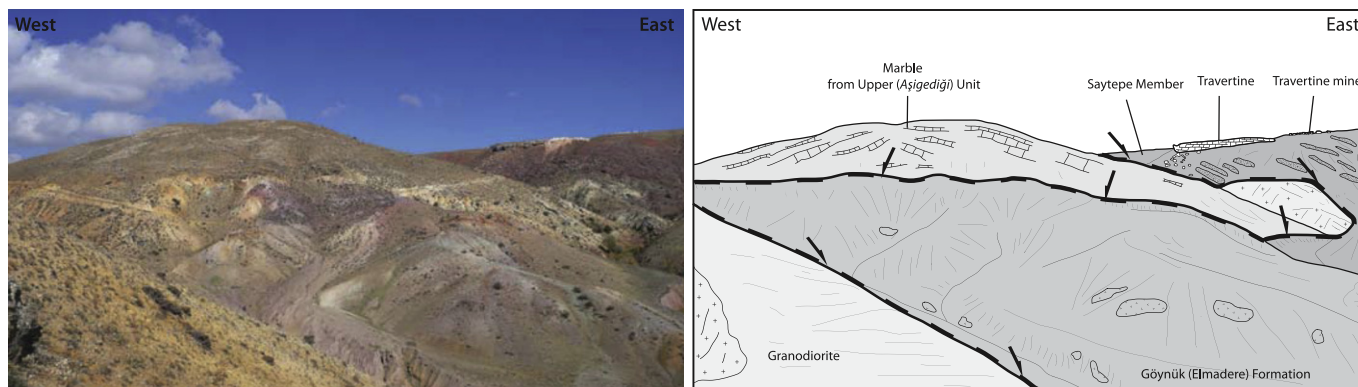


**Fig. 4.** Field aspect and interpretation of the tectonic contact, in the Gürleğen valley, between the Hırkadağ Massif and the Ayhan basin. Black arrows denote the trace and direction of motion of the fault.

### 3. Metamorphism of the Hirkadağ Massif

In order to complement and extend geographically the existing P–T estimates from the southern Hirkadağ Massif (Whitney and Dilek, 2001) we sampled metapelitic, quartzitic and calcsilicate rocks, equally distributed across the Hirkadağ Massif, to obtain insights in the metamorphic gradient across the area, mainly along SW–NE transects. We focused on three rock samples with pelitic compositions from the lower and intermediate structural unit and applied bulk-rock and mineral chemical analyses as well as conventional thermobarometry and thermodynamic modeling of phase assemblages to obtain quantitative estimates of the pressure and temperature conditions during HT metamorphism. The mineral abbreviations used below follow the nomenclature proposed by Whitney and Evans (2010).

#### 3.1. Petrology and texture

Thin sections of ten metamorphic rock samples were studied under the optical microscope to assess stable mineral assemblages and metamorphic grade (Table 1). The samples comprise five metapelites, one quartzite and four metacarbonates, widely distributed throughout the study area (Fig. 3).

##### 3.1.1. Metapelite samples

Three of the studied metapelitic samples (H2058C, H20C and H12G) belong to the lower unit, and two come from the intermediate unit (H19H and H2158B; Fig. 3).

The metapelitic rocks have a mineral assemblage consisting of  $\text{Sil} + \text{Grt} + \text{Qz} + \text{Bt} \pm \text{Ilm} \pm \text{Pl} \pm \text{Kfs}$ , partially replaced by a second assemblage of  $\text{Spl} + \text{Qz} \pm \text{Kfs} \pm \text{Grt} \pm \text{Crd} \pm \text{Pl} \pm \text{Sil}$ .

The schists have a marked foliation defined by biotite-rich domains with aggregates of fibrous and rare prismatic sillimanite and ilmenite. The matrix is dominated by quartz, with undulose extinction, and cordierite with relatively large idioblastic, xenoblastic or poikiloblastic garnet crystals (up to 1 cm) (Fig. 5a, b). Inclusions in garnets are  $\text{qtz} \pm \text{plag} \pm \text{bt} \pm \text{wh mica} \pm \text{sil} \pm \text{Kfs} \pm \text{spl}$ . Cordierite is present especially around garnet porphyroblasts, where highly resorbed garnet rims result from the replacement by cordierite and minor spinel (Fig. 5c, f). Garnet is surrounded by cordierite that shows symplectitic intergrowth with quartz at the contact with the garnet rim. The presence of cordierite near garnet is often associated with well-developed crystal faces of the garnet (Fig. 5c, f). Sillimanite shows two preferred orientations, which may be inherited from an earlier crenulation cleavage (similar observation was already reported by Whitney and Dilek (2001)). Spinel replaces fibrolite needles and seems to overgrow some biotite flakes with a preferred shape orientation (Fig. 5d). Spinel also occurs as a minor phase as inclusions within garnet and could be interpreted as texturally late as proposed by Whitney and Dilek (2001). In sample H12G, two generations of garnet have been recognized in thin section: an older xenoblastic garnet with no chemical zoning (12G3B) and a younger generation of smaller idioblastic garnet crystals with a zonation pattern

indicative for changing composition during growth (12G3A) (Fig. 5e). The younger garnet seems to replace biotite and contains inclusions of sillimanite. Potassium-feldspar is only present in small amounts and coexists with cordierite and minor quartz and plagioclase. In reaction rims around garnet, plagioclase is found as a reaction product together with spinel, quartz, biotite and subordinate amounts of K-feldspar and sillimanite. There is no significant variation in pelite mineral assemblages throughout the massif, as illustrated by sample H2158B (collected along the NE margin of the Hirkadağ Massif), which contains large poikiloblastic garnet surrounded by fibrolite and a matrix of quartz and potassic feldspar. Primary garnet and sillimanite are also partially replaced by cordierite and spinel, respectively (Fig. 5c).

##### 3.1.2. Quartzite

A sample (H20B) collected from a meter scale quartzitic band from the lower unit contains ~90–95% quartz coexisting with minor interstitial phyllosilicates, such as muscovite and chlorite. The large quartz grains are strongly affected by the pervasive development of “checkerboard type” subgrains. This textural observation was already reported from a garnet-biotite quartzite elsewhere in the Hirkadağ Massif (Whitney and Dilek, 2001).

##### 3.1.3. Metacarbonate

Four calcsilicate rocks were selected from the lower unit (H20D), two from the intermediate unit (H20E and H17E) and one from the upper unit (H11B) (Fig. 3).

The metacarbonates contain well-defined compositional banding with layers of equigranular calcite, diopside, plagioclase and titanite alternating with layers of plagioclase and quartz.

From the SW margin and lower unit of the massif (sample H20D), we recognize two generations of plagioclase based on microstructure and contact relationships. A first-generation of plagioclase occurs as inclusions in a second plagioclase. In the matrix, the second type of plagioclase is in apparent equilibrium with wollastonite and diopside. In the intermediate structural unit (sample H20E), the foliated calcsilicates contain layers with biotite, potassic feldspar and few epidote minerals. At the NE margin of the Hirkadağ Massif (samples H11B and H17E), both epidote and chlorite occur as local minor overgrowths on clinopyroxene. Rutile and scapolite are present as accessory phases.

#### 3.2. Mineral chemistry of metapelites

Three metapelitic schists from the lower and intermediate units (samples H20C, H12G and H19H Fig. 5a) were selected for detailed chemical analysis, as it preserves mineral assemblages representative of the peak metamorphic conditions in the Hirkadağ Massif. The mineral assemblage generally observed in the pelitic schists of the study area is: (1)  $\text{Sil} + \text{Grt} + \text{Qz} \pm \text{Pl} + \text{Bt} \pm \text{Ilm} \pm \text{Pl} \pm \text{Kfs}$ , partially overprinted by (2)  $\text{Spl} + \text{Qz} \pm \text{Kfs} \pm \text{Grt} \pm \text{Crd} \pm \text{Pl} \pm \text{Sil}$ .

Garnet, spinel, sillimanite, biotite, feldspar and cordierite were used for thermobarometric calculations described in paragraph 3.3. The

**Table 1**

Mineral compositions of samples analyzed in this study. Crosses denote the presence of a given mineral in the sample. Minor (accessory) phases are indicated with 'm'.

	Sample	Main minerals										Accessory phases									
		Grt	Spl	Bt	Sil	Pl	Kfs	Qz	Crd	Cal	Di	Chl	Ms	Scp	Ilm	Wo	Zrn	Ep	Crn	Rt	Ttn
MP	H12-G	x	x	x	m	x	x	x					m		x		x				
	H19-H	x	x	x	x	x	x	x					m		x				x		
	H20-C	x	m	m	x	x	x	x	x				m		x		x				
	K2058C	x	m	m	x		x	x	x						x		x				
	K2158B	x	x	x	x		x	x	x						x		x		x		
MC	H20B							x				x	x				x				
	H11B					x		x		x	x	m		m				m		x	x
	H17E					x		x		x	x	m		m				m		x	x
	H20D					x	x	m		x	x					x					x
	H20E			x		x	x	x		x	x							x			x



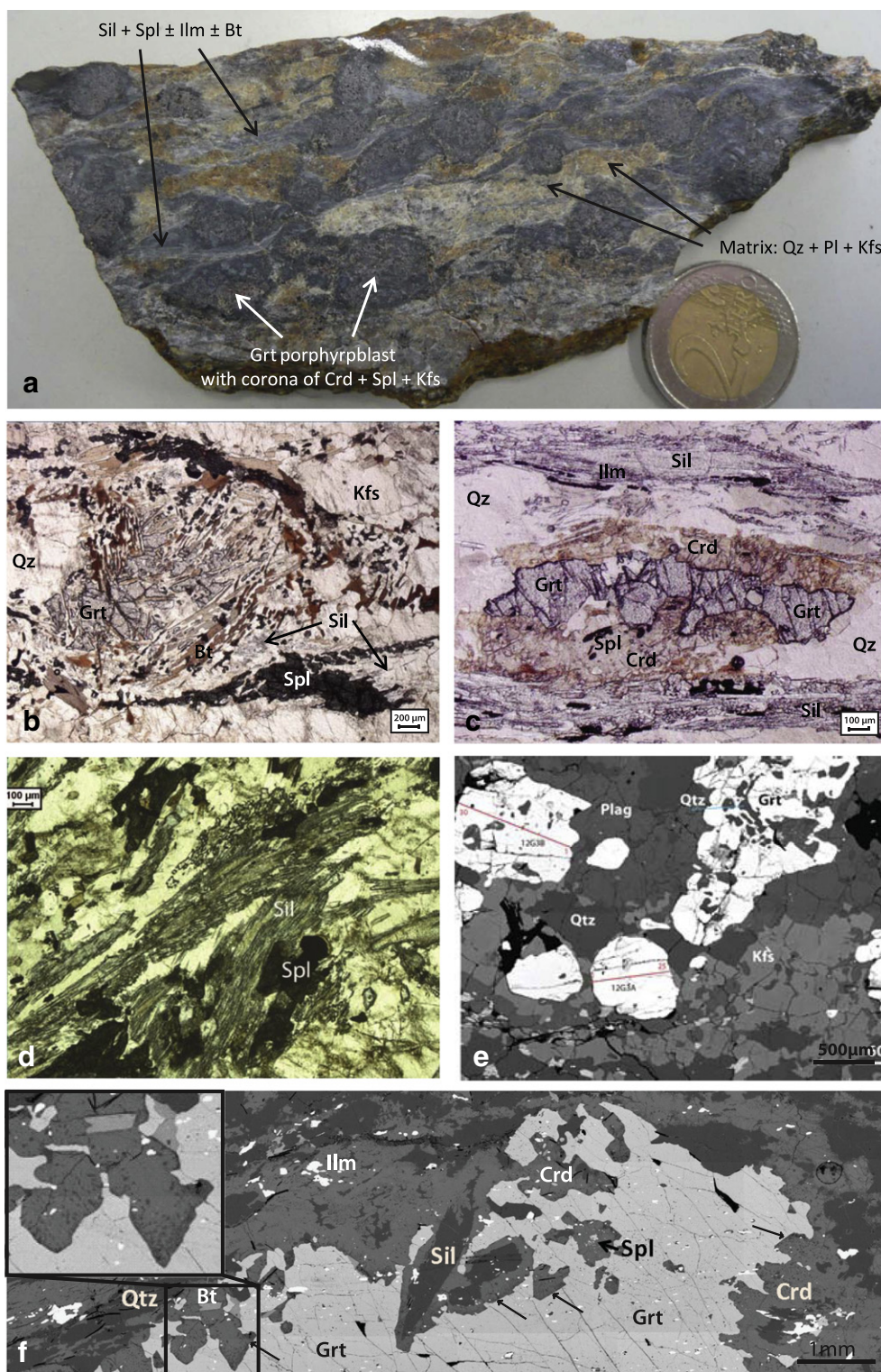


**Fig. 5.** a) Photograph of foliated sillimanite-bearing schist with large garnet porphyroblasts, sample H20C, b) micrograph showing typical mineral assemblage from metapelite sample H19H, c) micrograph of typical mineral assemblage in metapelite sample H2158B, d) micrograph showing spinel replacing fibrous sillimanite in sample H19H, e) Back-Scattered Electron image of the two generations of garnet in sample H12G (the position of the zoning profiles through garnets are indicated with red lines), and f) Back-Scattered Electron image of part of a cm-scale garnet in sample H20-C, showing reaction rim of cordierite surrounding the garnet with well-developed crystal faces (indicated with arrows).

chemical analyses were carried out using the JEOL JXA-8600 Superprobe at the Faculty of Geosciences at the University of Utrecht. The acceleration voltage during the analyses was 15 kV, at a beam current of 20 nA with a spot size of ~1–3 µm.

Garnet compositions are fairly similar for all analyzed grains and range within  $\text{Alm}_{67-86}\text{Gr}_{53-12}\text{Py}_{6-22}\text{Sp}_{1-3}$  (Table 2). Garnet shows a variety of zoning patterns. Larger xenoblastic garnet has no chemical zoning (12G3B) and smaller idioblastic garnet crystals (12G3A) exhibit

**Table 2**

Representative mineral compositions from samples H20C, H12G and H19H (oxides in wt%). The bottom part of the table displays the PT conditions calculated with various thermobarometers.

Sample mineral	H20C	H20C	H20C	H20C	H20C	H20C	H20C	H20C	H20C	H20C	H20C
	Grt core	Grt rim	Bt away Grt	Bt near Grt	Pl matrix	Kfs matrix	M matrix	Sil average	Ms matrix	Crd inclusions	Crd matrix
SiO <sub>2</sub>	37.83	37.26	34.32	35.37	56.59	63.22	0.01	36.33	45.07	47.55	46.91
Al <sub>2</sub> O <sub>3</sub>	20.92	20.80	17.89	17.20	26.97	18.73	57.21	62.69	34.74	32.54	32.10
FeO	34.21	38.02	22.24	18.07	0.15	0.00	36.61	0.32	1.44	10.82	12.60
MnO	0.65	0.75	0.02	0.03	0.01	0.00	0.01	0.00	0.00	0.08	0.09
MgO	3.76	2.89	7.57	10.70	0.01	0.00	2.42	0.01	0.64	6.92	5.58
CaO	3.12	1.06	0.00	0.00	8.85	0.12	n.a.	0.00	0.02	0.00	0.02
K <sub>2</sub> O	n.a.	n.a.	9.20	9.54	0.08	14.03	n.a.	0.01	9.90	0.00	0.13
Na <sub>2</sub> O	0.01	0.02	0.15	0.16	6.38	1.84	n.a.	0.00	0.66	0.07	0.10
TiO <sub>2</sub>	0.25	0.09	3.36	3.31	0.00	0.02	0.04	0.01	0.09	0.00	0.00
Cr <sub>2</sub> O <sub>3</sub>	0.01	0.01	0.06	0.05	0.01	0.00	0.17	0.04	0.00	0.00	0.01
V <sub>2</sub> O <sub>3</sub>	n.a.	n.a.	n.a.	n.a.	n.a.	n.a.	0.37	n.a.	n.a.	n.a.	n.a.
NiO	n.a.	n.a.	n.a.	n.a.	n.a.	n.a.	0.10	n.a.	n.a.	n.a.	n.a.
ZnO	n.a.	n.a.	n.a.	n.a.	n.a.	n.a.	3.37	n.a.	n.a.	n.a.	n.a.
Total	100.77	100.89	94.81	94.44	99.05	97.97	100.32	99.42	92.56	97.99	97.56
Si	3.00	2.99	2.67	2.71	2.56	2.96	0.00	0.99	3.08	4.97	4.97
Al	1.96	1.97	1.64	1.55	1.44	1.03	1.93	2.01	2.80	4.01	4.01
Fe-tot	2.27	2.56	1.45	1.16	0.01	0.00	0.88	0.01	0.08	0.95	1.12
Mn	0.04	0.05	0.00	0.00	0.00	0.00	0.00	0.00	0.00	0.01	0.01
Mg	0.45	0.35	0.88	1.22	0.00	0.00	0.10	0.00	0.06	1.08	0.88
Ca	0.27	0.09	0.00	0.00	0.43	0.01		0.00	0.00	0.00	0.00
K			0.91	0.93	0.00	0.84		0.00	0.86	0.00	0.02
Na	0.00	0.00	0.02	0.02	0.56	0.17		0.00	0.09	0.01	0.02
Ti	0.01	0.01	0.20	0.19	0.00	0.00	0.00	0.00	0.00	0.00	0.00
Cr	0.00	0.00	0.00	0.00	0.00	0.00	0.00	0.00	0.00	0.00	0.00
Zn							0.07				
Cations	8.00	8.02	7.78	7.80	5.00	5.00	3.00	3.01	6.99	11.03	11.04
X(Mg)	0.14	0.11	0.38	0.51			0.11			0.53	0.44
X(Fe)	0.75	0.84					0.89			0.47	0.56
X(Ca)	0.09	0.03			XAn: 0.43	XAn: 0.01					
X(Mn)	0.01	0.02			XOr: 0.01	XOr: 0.83					
Fe/(Fe + Mg)	0.84	0.88			XAb: 0.56	XAb: 0.16					
Thermo/Baro	Assembl.	GB (°C)	GC (°C)	GASP (kbar)	GPMB-Fe (kbar)	GPMB-Mg (kbar)	Average P (kbar)				
H20C	1	742		7.99	9.45	6.91	8.12				
H20C	2	520	702				ca. 3–4				
Sample mineral	H12G	H12G	H12G	H12G	H12G	H12G	H12G	H12G	H12G	H12G	H12G
	Grt3A core	Grt3A rim	Grt3A average	Bt matrix	Pl matrix	Kfs matrix	Kfs inclusion	Spl matrix	Sil inclusion	Sil matrix	
SiO <sub>2</sub>	38.30	38.34	37.81	33.93	61.33	62.94	63.10	0.01	36.24	35.77	
Al <sub>2</sub> O <sub>3</sub>	20.93	21.17	20.95	18.27	23.17	18.73	18.77	59.12	62.81	61.90	
FeO	31.09	33.37	33.51	17.63	0.07	0.05	0.52	35.71	0.88	0.25	
MnO	1.34	1.42	1.41	0.08	0.02	0.00	0.02	0.15	0.04	0.01	
MgO	4.81	5.72	5.64	9.03	0.00	0.00	0.01	4.45	0.01	0.01	
CaO	4.46	1.04	0.89	0.30	4.50	0.22	0.12	n.a.	0.00	0.01	
K <sub>2</sub> O	n.a.	n.a.	n.a.	8.20	0.28	13.46	13.84	n.a.	0.00	0.01	
Na <sub>2</sub> O	0.02	0.01	0.01	0.14	8.76	2.22	1.93	n.a.	0.01	0.00	
TiO <sub>2</sub>	0.07	0.01	0.03	4.50	0.02	0.04	0.04	0.04	0.02	0.01	
Cr <sub>2</sub> O <sub>3</sub>	0.00	0.01	0.01	0.02	0.00	0.00	0.01	0.04	0.02	0.01	
V <sub>2</sub> O <sub>3</sub>	n.a.	n.a.	n.a.	n.a.	n.a.	n.a.	n.a.	0.11	n.a.	n.a.	
NiO	n.a.	n.a.	n.a.	n.a.	n.a.	n.a.	n.a.	0.00	n.a.	n.a.	
ZnO	n.a.	n.a.	n.a.	n.a.	n.a.	n.a.	n.a.	0.73	n.a.	n.a.	
Total	101.02	101.08	100.25	92.10	98.14	97.67	98.35	100.35	100.03	97.97	
Si	3.01	3.01	3.00	2.65	2.77	2.95	2.94	0.00	0.98	0.99	
Al	1.94	1.96	1.96	1.68	1.23	1.03	1.03	1.95	2.01	2.01	
Fe-tot	2.04	2.19	2.22	1.15	0.00	0.00	0.02	0.84	0.02	0.01	
Mn	0.09	0.09	0.09	0.01	0.00	0.00	0.00	0.00	0.00	0.00	
Mg	0.56	0.67	0.67	1.05	0.00	0.00	0.00	0.19	0.00	0.00	
Ca	0.38	0.09	0.08	0.02	0.22	0.01	0.01	0.00	0.00	0.00	
K				0.82	0.02	0.80	0.82	0.00	0.00	0.00	
Na	0.00	0.00	0.00	0.02	0.77	0.20	0.17	0.00	0.00	0.00	
Ti	0.00	0.00	0.00	0.26	0.00	0.00	0.00	0.00	0.00	0.00	
Cr	0.00	0.00	0.00	0.00	0.00	0.00	0.00	0.00	0.00	0.00	
Zn								0.02			
Cations	8.02	8.01	8.02	7.67	5.00	5.00	5.00	3.00	3.01	3.01	
X(Mg)	0.18	0.22	0.22	0.48				0.18			
X(Fe)	0.67	0.72	0.73					0.82			
X(Ca)	0.12	0.03	0.02		XAn: 0.22	XAn: 0.01	XAn: 0.01				
X(Mn)	0.03	0.03	0.03		XOr: 0.02	XOr: 0.79	XOr: 0.82				
Fe/(Fe + Mg)	0.78	0.77	0.77		XAb: 0.77	XAb: 0.20	XAb: 0.17				
Thermo/Baro	Assembl.	GB (°C)	GASP (kbar)	GPMB-Fe (kbar)	GPMB-Mg (kbar)	Average P (kbar)					

(continued on next page)



Table 2 (continued)

H12G	1	729	2.67	2.67								
Sample mineral	H19H Grt1A core	H19H Grt1A rim	H19H Grt1C core	H19H Grt1C rim	H19H Bt inclusion	H19H Bt matrix	H19H Pl inclusion	H19H Pl matrix	H19H Kfs inclusion	H19H Kfs matrix	H19H Spl matrix	H19H Sil matrix
SiO <sub>2</sub>	36.84	36.96	37.51	37.68	32.88	33.27	58.43	60.43	63.01	62.52	0.01	35.81
Al <sub>2</sub> O <sub>3</sub>	20.42	20.18	20.52	20.70	17.68	20.14	25.31	23.98	18.63	18.70	58.14	62.07
FeO	39.02	36.77	38.91	36.82	20.84	20.43	0.56	0.18	0.41	0.29	37.85	0.27
MnO	0.44	0.70	0.35	0.81	0.02	0.05	0.02	0.01	0.00	0.01	0.11	0.01
MgO	1.84	2.71	1.63	3.15	7.79	7.44	0.00	0.00	0.02	0.00	3.67	0.01
CaO	2.05	2.90	2.63	2.02	0.01	0.00	6.96	5.16	0.06	0.08	n.a.	0.01
K <sub>2</sub> O	n.a.	n.a.	n.a.	n.a.	9.04	9.60	0.28	0.22	14.70	14.17	n.a.	0.01
Na <sub>2</sub> O	0.01	0.01	0.01	0.01	0.30	0.16	7.34	8.37	1.51	1.82	n.a.	0.00
TiO <sub>2</sub>	0.03	0.06	0.04	0.05	5.40	3.22	0.02	0.03	0.03	0.01	0.05	0.01
Cr <sub>2</sub> O <sub>3</sub>	0.00	0.01	0.00	0.00	0.00	0.00	0.01	0.01	0.00	0.00	0.01	0.00
V <sub>2</sub> O <sub>3</sub>	n.a.	n.a.	n.a.	n.a.	n.a.	n.a.	n.a.	n.a.	n.a.	n.a.	0.06	n.a.
NiO	n.a.	n.a.	n.a.	n.a.	n.a.	n.a.	n.a.	n.a.	n.a.	n.a.	0.01	n.a.
ZnO	n.a.	n.a.	n.a.	n.a.	n.a.	n.a.	n.a.	n.a.	n.a.	n.a.	0.07	n.a.
Total	100.65	100.31	101.58	101.24	93.94	94.30	98.92	98.38	98.37	97.61	99.99	98.20
Si	2.99	2.99	3.01	3.01	2.58	2.59	2.64	2.73	2.94	2.93	0.00	0.99
Al	1.96	1.93	1.94	1.95	1.63	1.85	1.35	1.28	1.03	1.03	1.94	2.01
Fe-tot	2.65	2.49	2.61	2.46	1.37	1.33	0.02	0.01	0.02	0.01	0.90	0.01
Mn	0.03	0.05	0.02	0.05	0.00	0.00	0.00	0.00	0.00	0.00	0.00	0.00
Mg	0.22	0.33	0.20	0.38	0.91	0.86	0.00	0.00	0.00	0.00	0.16	0.00
Ca	0.18	0.25	0.23	0.17	0.00	0.00	0.34	0.25	0.00	0.00		0.00
K					0.90	0.95	0.02	0.01	0.88	0.85		0.00
Na	0.00	0.00	0.00	0.00	0.04	0.02	0.64	0.73	0.14	0.17		0.00
Ti	0.00	0.00	0.00	0.00	0.32	0.19	0.00	0.00	0.00	0.00	0.00	0.00
Cr	0.00	0.00	0.00	0.00	0.00	0.00	0.00	0.00	0.00	0.00	0.00	0.00
Zn											0.00	
Cations	8.03	8.04	8.02	8.02	7.76	7.79	5.01	5.01	5.00	5.00	3.00	3.01
X(Mg)	0.07	0.10	0.06	0.12	0.40	0.39					0.15	
X(Fe)	0.86	0.80	0.85	0.80							0.85	
X(Ca)	0.06	0.08	0.07	0.06			XAn: 0.33	XAn: 0.25	XAn: 0.00	XAn: 0.00		
X(Mn)	0.01	0.02	0.01	0.02			XOr: 0.02	XOr: 0.01	XOr: 0.86	XOr: 0.83		
Fe/(Fe + Mg)	0.92	0.88	0.93	0.87			XAb: 0.65	XAb: 0.74	XAb: 0.13	XAb: 0.16		
Thermo/Baro	Assembl.	GB	GASP	GPMB-Fe	GPMB-Mg	Average P						
		(°C)	(kbar)	(kbar)	(kbar)	(kbar)						
H19H	0	526	3.63	5.01	3.54	4.06						
H19H	1	624	7.84	9.08	7.04	7.98						

a zonation pattern in which cores are richer in Ca and Mn than rims, Fe and Mg increase and Fe/(Fe + Mg) ratio decreases toward the garnet rim, which suggests increasing temperature during garnet growth (Spear, 1993). The presence of cordierite and the newly grown crystal faces at the contact between cordierite and garnet suggest that the core composition of this garnet reflects near-peak temperatures and the rim reflects retrograde conditions. Spinel from the matrix is rich in iron and has a composition close to the hercynite endmember FeAl<sub>2</sub>O<sub>4</sub>, with small amounts of Mg (11 < Mg# < 18) and Zn (0.1 < wt% ZnO < 3.4; Table 2). The Fe and Mg content of biotite in the Hirkadağ samples varies from 0.49 < Fe/(Fe + Mg) < 0.62. Feldspar compositions are Ab<sub>56–74</sub>An<sub>25–43</sub>Or<sub>1–2</sub> for plagioclase and Ab<sub>13–20</sub>An<sub>0–1</sub>Or<sub>79–86</sub> for K-feldspar (Table 2). Representative compositions of cordierite in the matrix and inclusions in garnet for sample H20C are given in Table 2. The X<sub>Mg</sub> (Mg/Mg + Fe<sup>2+</sup>) ratio in cordierite in inclusion ranges from 47 to 53 and 44 to 56 in the matrix.

### 3.3. Pressure–temperature conditions

Based on mineral chemistry data, equilibrium temperature estimates were calculated using the garnet–biotite (GB) exchange thermometer (Bhattacharya et al., 1992). Pressure is calculated with the garnet–aluminosilicate–silica–plagioclase (GASP) and the garnet–plagioclase–muscovite–biotite (GPMB–Fe and GPMB–Mg) net transfer barometers (Ghent and Stout, 1981; McKenna and Hodges, 1988). The estimated values for temperature and pressure conditions of equilibration are given in Table 2 and marked with black dots in the PT diagram (Fig. 6).

For the previously described H20C and H19H metapelitic sample, calculated equilibrium conditions for the early mineral assemblage, including data from garnet cores, are 740 and 620 °C respectively (GB thermometer) and 8 kbar (average pressure of GASP, GPMB–Fe and GPMB–Mg barometers; Table 2). Calculations with garnet rim compositions and associated biotite give an equilibrium temperature of 520 and 730 °C (GB thermometer) and 700 °C using the garnet rim and cordierite matrix compositions (Grt–Crd thermometer (Bhattacharya et al., 1988)), while the pressure is estimated around 3–4 kbar based on the occurrence of cordierite as replacement of garnet (Spear and Cheney, 1989) (Table 2).

### 3.4. Bulk rock composition and thermodynamic modeling

The bulk rock composition of the samples H20C, H12G and H19H has been determined by X-ray fluorescence (Thermo ARL 9400 XRF) on fused glass beads and pressed powder pellets at Utrecht University. The resulting major element compositions shown in Table 3 are used to calculate the stability fields of mineral assemblages in a specified PT space, via the construction of PT-fixed-composition phase diagram sections (or pseudosections) using the Theriak/Domino software package (de Capitani, 1994; de Capitani and Petrakakis, 2010). We chose to run the calculations for the CNKFMASH system as we are dealing with rocks of metapelitic affinity and used the thermodynamic database (tcd55c2d.bs) based on Holland and Powell (1998). For the calculations, a surplus amount of water is added, to permit the occurrence of hydrous minerals like micas and cordierite.

Fig. 6 presents the modeled Domino pseudosections with the stability fields of all stable mineral assemblages for a PT-space ranging from

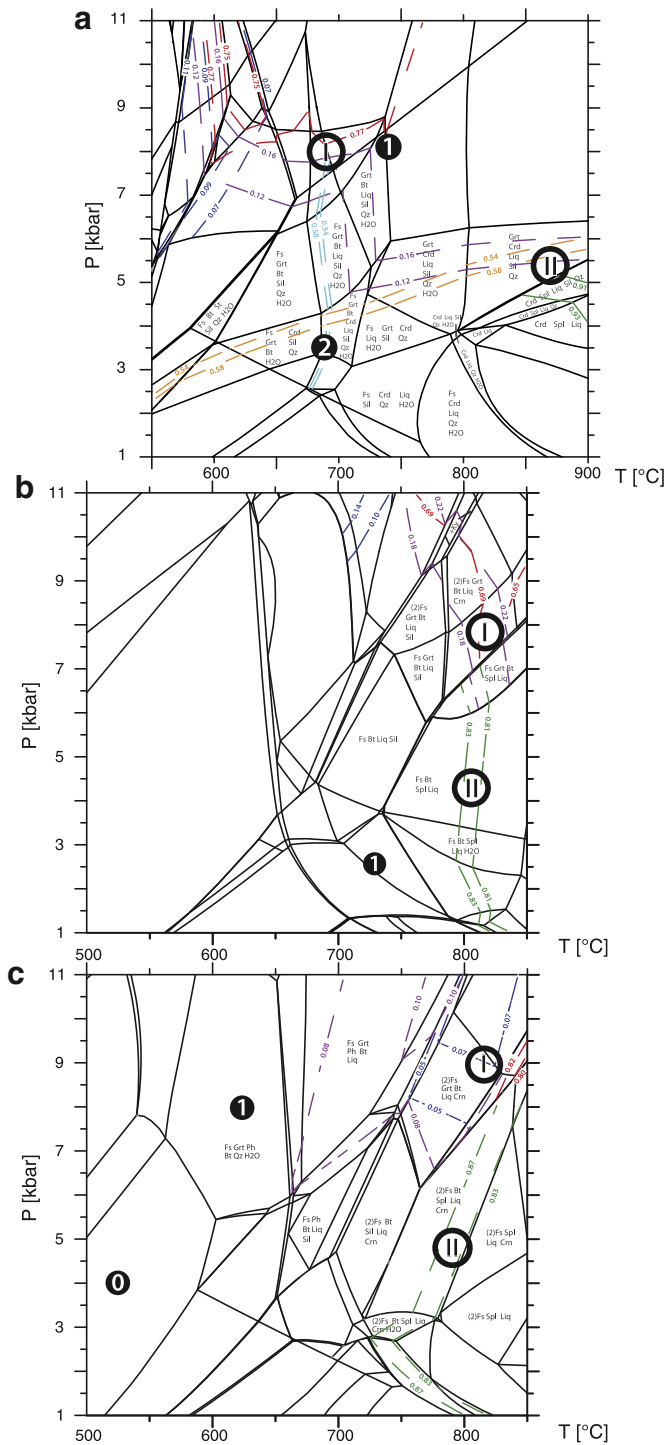


**Fig. 6.** CNKFMASH pseudosection calculated with Domino for the bulk rock composition of samples H20C (a), H12G (b) and H19H (c) with water added. The relative proportion of the elements used as input for Domino calculations can be found in Table 3. The main mineral assemblages are listed in the diagram. The colored dotted lines and associated numbers represent the calculated isopleths and respective values (red: almandine, purple: pyrope, blue: grossular, cyan: albite, orange: cordierite and green: hercynite). The PT fields where the described assemblages are proposed to be stable are numbered in Roman number, referring respectively to an early and late mineral assemblages. Estimates calculated using conventional thermobarometry are plotted as numbers with black circles.

500 to 900 °C and 1–11 kbar. On the PT pseudosection, the stability fields are labeled with their mineral assemblages. The inferred stable PT domains are shown in Fig. 6 (with Roman numbers) and compared

**Table 3**

XRF analyses for the samples H20C, H12G and H19H. Analyses in wt% and normalized to 100%, assuming that  $\text{Fe}_{\text{total}} = \text{Fe}^{2+}$ .

Sample name		H20C	H12G	H19H
SiO <sub>2</sub>	wt%	62.94	61.70	49.78
AlO <sub>3</sub>	wt%	21.95	19.44	29.20
TiO <sub>2</sub>	wt%	1.49	0.86	1.10
FeO	wt%	9.17	5.78	8.34
MnO	wt%	0.12	0.15	0.08
CaO	wt%	0.55	1.09	0.68
MgO	wt%	1.30	1.38	0.99
Na <sub>2</sub> O	wt%	0.53	3.53	2.68
K <sub>2</sub> O	wt%	1.95	6.06	7.15
Total		100	100	100

with the PT-estimates obtained with thermobarometry (with black circles). In the pseudosection of sample H20C (Fig. 6a), the location in PT-space of the first assemblage is assessed by determining the best intersection fit between the isopleths of almandine, pyrope and grossular in garnet core, and albite in plagioclase. In this case, the  $\text{Alm}_{0.14}$ ,  $\text{Prp}_{0.75}$  and  $\text{Ab}_{0.56}$  isolines intersect near the recognized stable assemblage suggesting PT conditions at about 8 kbar and 700 °C. We note that the  $\text{Gr}_{0.09}$  isopleth does not reach the proposed PT domain and plots at lower temperatures. This difference may be caused by the effect of small but significant amounts of, for example spessartine in garnet, which is not considered in the solid solution model used for thermodynamic modeling.

Microstructural relationships show that the first assemblage is partly replaced by a second assemblage ( $\text{Grt} \rightarrow \text{Crd} + \text{Qz}$  and  $\text{Sil} \rightarrow \text{Spl}$ ). The replacement of garnet by cordierite occurs at about 4 kbar. The growth of spinel ( $\text{Hc}_{0.89}$ ) indicates heating to at least 850 °C, with the appropriate isopleth at even higher temperatures. The thermobarometric calculation for the first mineral assemblage plots near the PT path inferred from Domino calculations (1 in Fig. 6a). For the second mineral assemblage, the peak temperature of >850 °C based on the occurrence of spinel and cordierite inferred from the Domino pseudosection is estimated at about 700 °C using the garnet–cordierite geothermometer.

In the pseudosection of sample H12G (Fig. 6b), the PT domain of assemblage I (constrained by the  $\text{Alm}_{0.67}$  and  $\text{Prp}_{0.18}$  isopleths) suggests conditions around 800 °C and ~9 kbar. In this case too, the  $\text{Gr}_{0.12}$  isopleth does not cross the proposed stability field but plots at higher pressure and lower temperature. Domain II is defined by the appearance of spinel and restricted by the spinel  $\text{Hc}_{0.82}$  isopleth and ranges at ~800 °C and ~5 kbar. The estimate for peak metamorphic conditions obtained by thermobarometric calculation indicates lower PT conditions than those indicated in the domain of stable assemblage (1 in Fig. 6b).

In the pseudosection of sample H19H (Fig. 6c), the conditions of the PT domains I and II (restricted by the  $\text{Alm}_{0.80}$ ,  $\text{Prp}_{0.10}$ ,  $\text{Gr}_{0.07}$  and  $\text{Hrc}_{0.85}$  isolines respectively) resemble those of H12G with a temperature around 800 °C and a pressure of ~8–9 and 4 kbar, respectively. However, the thermobarometric calculation for the peak mineral assemblage (1 in Fig. 6c) plots at a lower temperature of about 600 °C and 8 kbar.

The high temperature conditions inferred from the output of thermodynamic calculations and thermobarometry suggest that the rock likely underwent some degree of partial melting. However, direct evidence for the presence of a melt within the high grade metapelites is difficult to assess. As reported in the literature, some quartzofeldspathic layers may represent anatectic leucosomes from migmatitic segregations but later deformation makes their structural interpretation debatable (Whitney and Dilek, 2001). Alternatively, the presence of a melt may be evidenced by the K-feldspar + quartz ( $\pm$  plagioclase)-rich zones separated from zones rich in aluminous minerals like Sil, Crd, Grt and Bt, and by the well developed crystal faces at the boundary between primary garnet and secondary cordierite (Fig. 5c, f), suggestive of an environment with an interstitial liquid phase (MacKenzie and Adams, 2003).



#### 4. Structural analysis of the Hırkadağ Massif

##### 4.1. Overall structure

The structure of the Hırkadağ Massif is illustrated in Fig. 7 showing a compilation of data collected by Aydın (1985) in the area west of the Kırşehir–Nevşehir road, and Teklehaimanot (1993) for the eastern part, complemented with our own measurements across the Hırkadağ Massif. The rocks have a pervasive metamorphic foliation ( $S_m$ ), that is almost always parallel to the original sedimentary bedding ( $S_0$ ). Pelitic rocks from the lower unit exposed along the SW margin preserve well-developed, intense ductile deformation features. The quartz-rich sillimanite- and garnet-bearing schists have a strongly developed cleavage, which is sometimes truncated by large garnet porphyroblasts. The main foliation  $S_m$  is associated with the peak metamorphic mineral assemblage of Sil + Grt + Qz ± Kfs ± Bt ± Ilm (Fig. 5a and c). Pure quartzite occurs as massive meter-scale bands without a clear foliation. Toward the NE and upward in the succession, the more calcareous lithologies do not preserve evidence of ductile deformation, presumably because pervasive recrystallization affected these calcite-rich compositions. Calc-silicates and banded impure marbles often appear as competent layers from a few to hundreds of meters thick. Massive marbles alternating with meter-scale calc-silicate bands from the upper unit in

the northeast show a consistent orientation of dipping layers, striking parallel to the contact with the Büyükkışla basin. The main trend of the pervasive  $S_m$  foliation is NW–SE, with approximately NE-directed dips. In metapelite compositions, stretched sillimanite and biotite form lineations on the foliation planes, while in the metacarbonates elongated amphibole and some pyroxene define a stretching lineation. The main trend of these lineations is around N120–150, and few identifiable kinematic indicators show a top-to-the-SE sense of shear (black lines in Fig. 7). Competent calc-silicate beds are boudinaged and foliation boudinage occurs at the necks of the boudins (Fig. 8a). In the SW, foliated calc-silicates deformed into various types of folds, ranging from tight to isoclinal symmetric and asymmetric folds. The general strike of axial planes of the isoclinal folds and the boudinage neck lines coincides with the orientation of the regional foliation ( $S_m$ ) and suggests that these folds and boudinage result from the same deformation phase ( $F_m$ ).

In some localities,  $S_m$  and associated  $F_m$  are refolded into meter-scale tight folds (Fig. 8b, d). This refolding phase has led to the formation of a new axial planar foliation (referred to as  $S_m + 1$ ). This secondary structure is characterized by the presence of relatively open folds, has shallower dips than  $S_m$ , and presents a general WNW–ESE strike alternatively dipping toward the ENE and WSW. The scale of these younger folds varies from cm to hundreds of meters in wavelength. In the SW of the study area, a 5–10 cm wide aplitic dyke cuts the  $S_m$  foliation, but

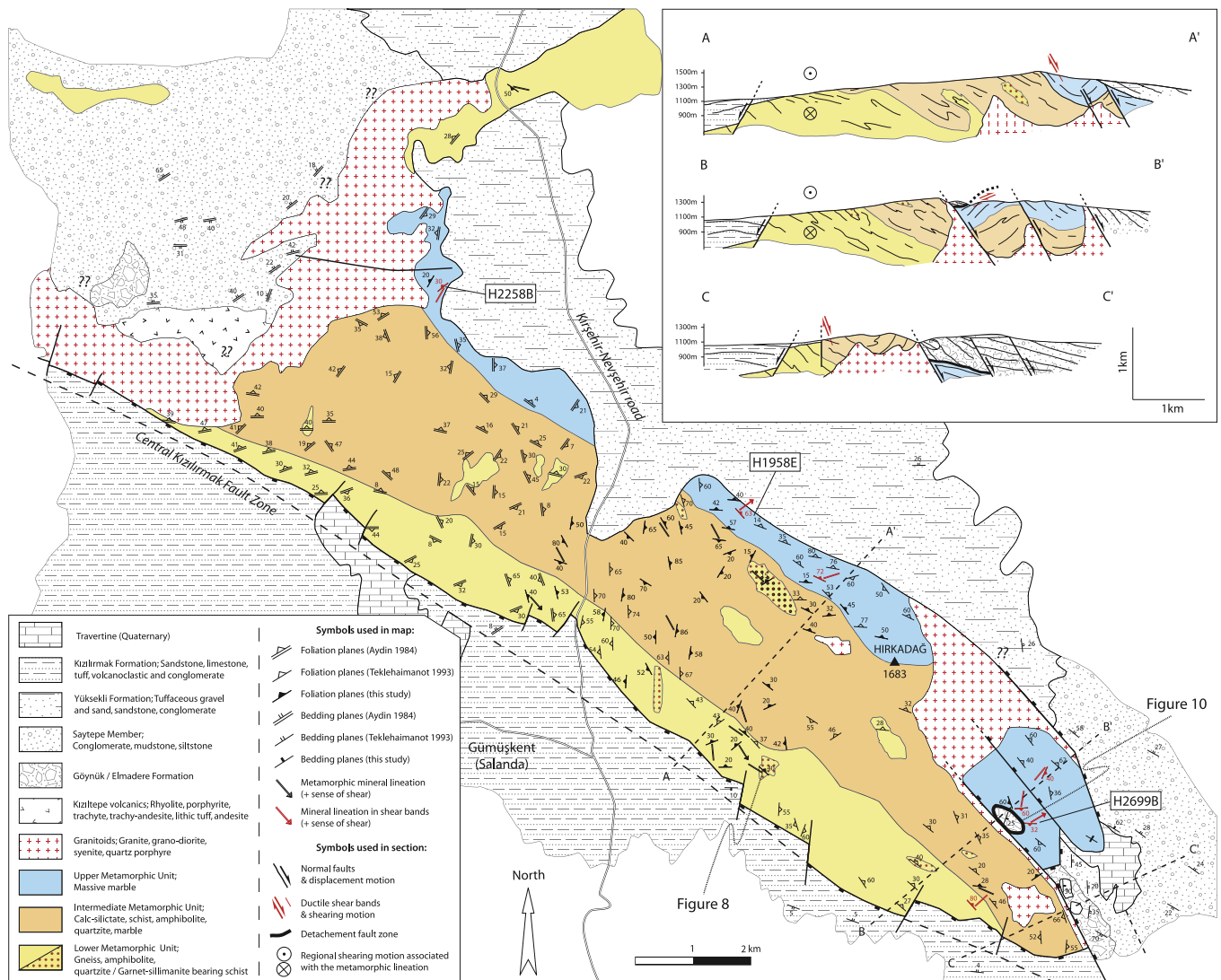


**Fig. 7.** Detailed structural map of the Hırkadağ Massif showing bedding, foliation planes and mineral lineations in both HT and mylonitic rocks from this study, supplemented with literature data. Three SW–NE cross-sections through the Hırkadağ Massif are presented. Locations of marble samples with mylonitic shear bands are shown.

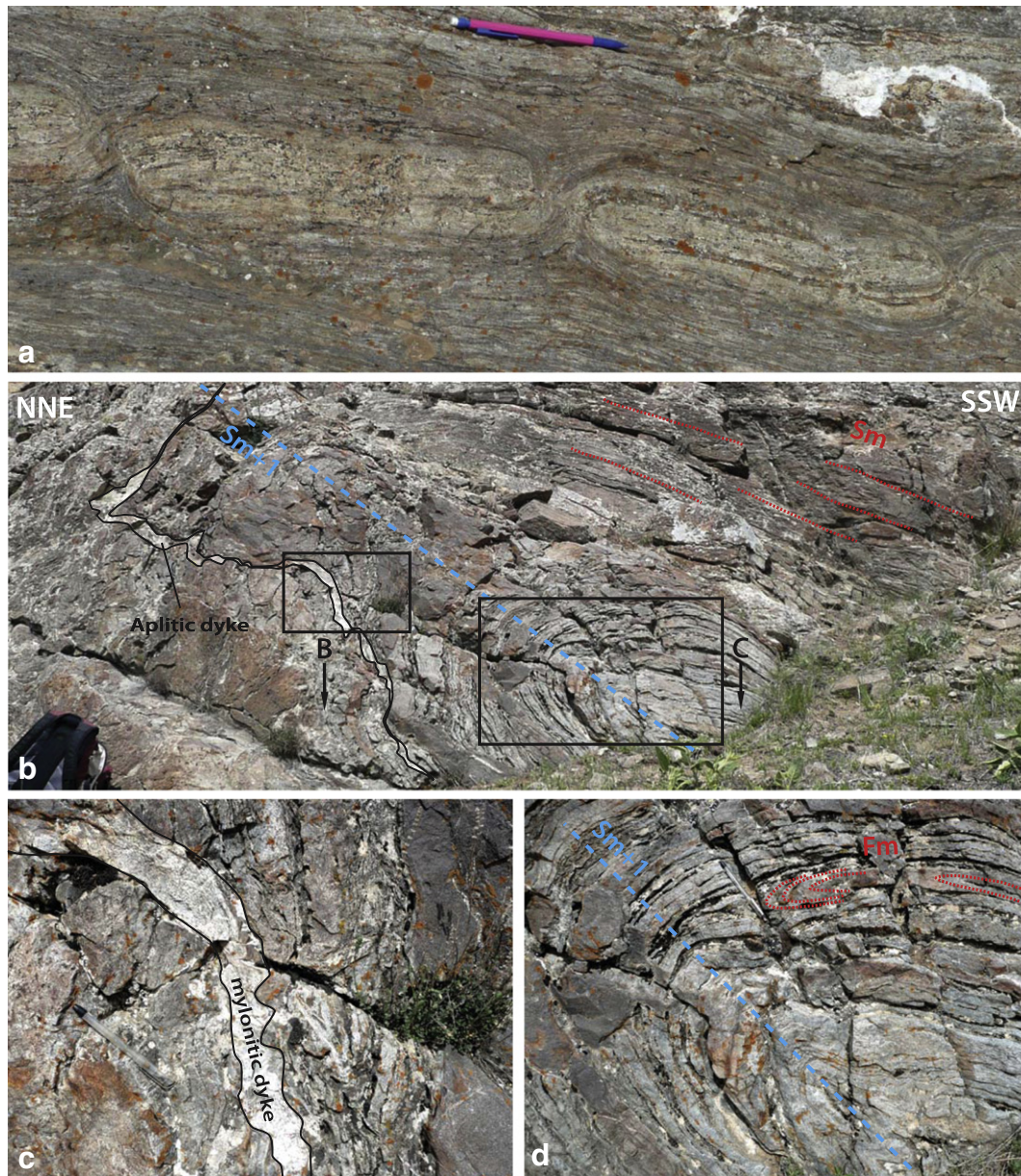


**Fig. 8.** a) Boudinage in layered calcilicates of the Hırkadağ Massif. b–c–d) Field aspects of structures depicting the relationships between folds of different generations and cross-cutting aplitic dykes from the SW margin of the Hırkadağ Massif. See text for further explanation.

becomes progressively mylonitized at the hinge of the  $S_m + 1$  folds (Fig. 8c). This relationship suggests that intrusion of the aplitic dyke and the  $S_m + 1$  deformation phase may have been coeval. Note, however, that this observation was made at only one specific locality, and it remains unclear whether such a relationship between aplite injection and deformation holds for the entire Hırkadağ Massif.

Within the northern area, massive marbles of the upper unit display another type of deformation. The large meter-scale beds made up of coarse-grained calcite are locally cross-cut by protomylonitic to mylonitic shear bands ranging from 1 to 10 cm wide (Fig. 7). The mylonitic shear bands strike mostly parallel to the main foliation but the dips are steeper and range around  $60^\circ$  NE, such that they cut the main foliation. Sparse mylonitic lineations are oriented  $\sim 40^\circ$ – $60^\circ$ . The microstructure and fabric of three selected calcite shear bands in samples H2258B, H1958E, and H2699B have been studied by optical microscopy (Fig. 9).

The shear bands are developed in nearly pure carbonates, with few grains of recrystallized quartz, muscovite and chlorite suggesting greenschist facies retrograde conditions during localized deformation. Moreover, the development of mylonites in calcite-rich rocks is characteristic of relatively low temperature conditions (de Bresser et al., 2002). Microstructurally the shear bands are characterized by large  $\sigma$ -type, or even fish-type calcite porphyroclasts surrounded by very small calcite grains, organized in fine bands between the porphyroclasts. The fine-grained bands define the main shear plane (Fig. 9). Within the elongated large calcite porphyroclasts, we observe a clear network of two sets of bent and curved twins, of which one set is better developed. The consistent obliquity of the twins with respect to the planes of grain size reduction may be used as an indicator to determine the shear sense (Bestmann et al., 2000). Both calcite twin obliquity and  $\sigma$ -type porphyroclasts point to a normal top-to-NE ( $\sim 40^\circ$ – $60^\circ$ ) shear motion. Although the three selected samples show different degrees of dynamic recrystallization, the sense of shear in the three samples consistently



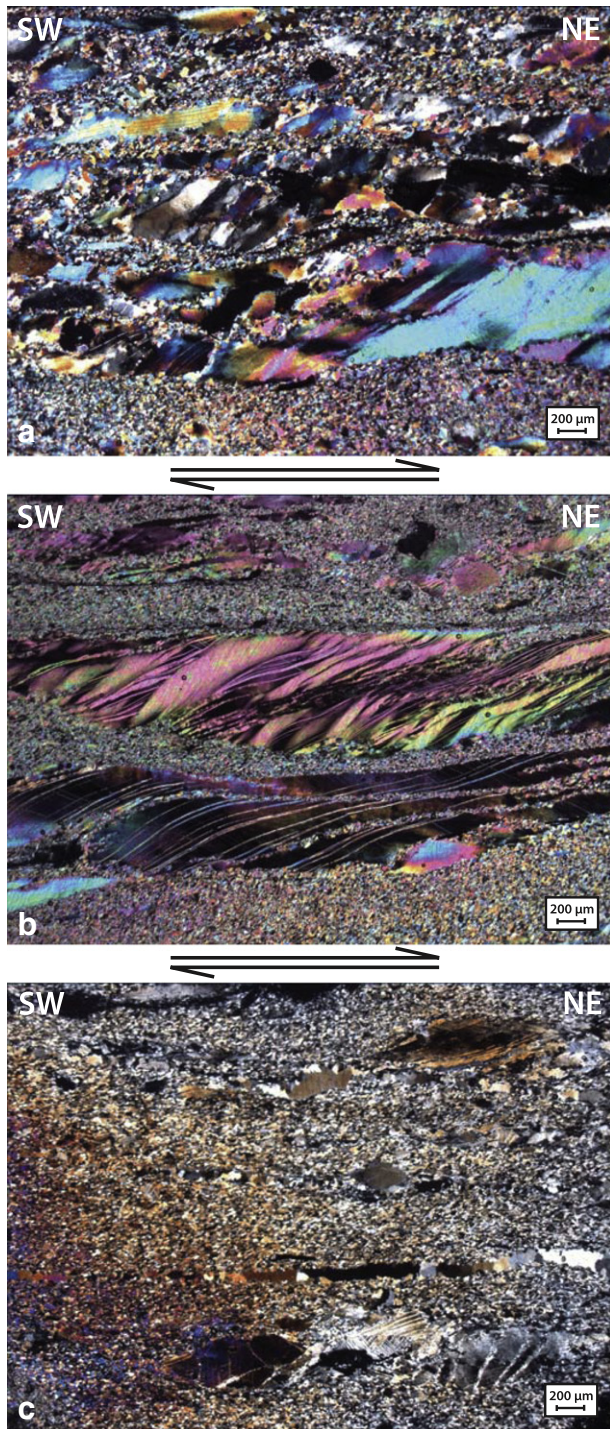


**Fig. 9.** Micrographs showing mylonitic shear bands from the marble-rich northern border of the Hırkadağ Massif. Locations of the samples are shown in Fig. 7; a) sample H2258B, b) sample H1958E, and c) sample H2699B. Arrows denote inferred shear senses.

indicates a consistent top-to-the-NE motion along the NE marble-rich margin of the Hırkadağ Massif (Fig. 9). Mylonites in the upper carbonates are also associated with cataclasites in a locality in the east of the Hırkadağ Massif, in the Sığırkalan area, which we studied in detail as described below.

#### 4.2. The Sığırkalan area

The eastern contact of the Hırkadağ Massif with the Ayhan basin is defined by NW–SE striking high-angle normal faults. The Sığırkalan

area (Fig. 10a) is located in the footwall of the basin-bounding fault, and represents a back-tilted fault block. In the NE, massive marbles of the upper metamorphic unit form a large antiform that plunges toward the SW below a klippe of non-metamorphosed sedimentary rocks. At the contact, marbles are intensely mylonitized and overprinted by several meters of cataclasites and breccias, associated with a brown to yellow-colored matrix with secondary mineral phases such as quartz and dolomite (Fig. 10b). Fragments in the breccia include the marble-rich protolith with mylonitic and protomylonitic bands (Fig. 10d). Above the cataclastic marbles there are purple conglomerates that contain pebbles exclusively consisting of dark-colored volcanic rocks (Fig. 10c) and no trace of pebbles derived from metamorphic source rocks. The pebbles in the purple conglomerates closely resemble the stratigraphically lowest unit of the Ayhan Basin, which contains syn-sedimentary intercalated ~72 Ma old andesitic lavas (Advokaat et al., 2014). The conglomerates preserve bedding planes which are shallowly dipping toward the SW and locally are displaced by faults (Fig. 10b). Taken together, this contact, which is obviously tectonic, involves a ductile-to-brittle shear-zone in the footwall marbles, and a non-metamorphosed conglomerate containing volcanic pebbles of most likely late Cretaceous age (~72 Ma) and lacking any metamorphic debris in the hanging wall.

## 5. Discussion

Below we integrate the results from our metamorphic and structural study together with the geochronological data reported in Lefebvre (2011) from the Hırkadağ Massif to infer its tectono-metamorphic evolution and its position within the regional evolution of the CACC.

### 5.1. The tectonic history of the Hırkadağ Massif

Chronological constraints on cooling of the high-grade metamorphic and intrusive rocks are reported in Lefebvre (2011). They dated (1) the granodioritic pluton that intruded in the NE of the Hırkadağ Massif by titanite U/Pb dating (sample [H2699C] in Fig. 3) and (2) the garnet-sillimanite schist of the lowermost formation, using K-feldspar and biotite  $^{40}\text{Ar}/^{39}\text{Ar}$  analysis (sample [H19H] in Figs. 3 and 5b).

The dated granodiorite is mostly composed of feldspar, quartz, altered phyllosilicates and idiomorphic titanite crystals. The data yields a U–Pb concordia age of  $77.2 \pm 0.4$  Ma (Figs. 2.11a–b in Lefebvre (2011)), which dates at least the time of cooling below ~700–660 °C; (Scott and St-Onge, 1995). For the metapelite,  $^{40}\text{Ar}/^{39}\text{Ar}$  analysis on biotites (estimated closure temperature of ~300–350 °C (Grove and Harrison, 1996)) produced a plateau age of  $68.8 \pm 0.9$  Ma, while K-feldspars (estimated closure temperature of ~200–250 °C (Harrison and McDougall, 1982; McDougall and Harrison, 1999)) yielded a plateau age of  $67.0 \pm 1.2$  Ma (Figs. 2.11c–d in Lefebvre (2011)).

The structural, metamorphic and geochronological data presented above can be summarized in a P–T–t evolution of the Hırkadağ metamorphic rocks. The initial HT metamorphic conditions reached ~7–8 kbar/700 °C and were associated with isoclinal folding, the formation of the main pervasive foliation, and top-to-the-SE HT shearing. These inferred regional metamorphic conditions correspond to the upper amphibolite facies. In contradiction with previous studies, no major differences in metamorphic grade have been identified in this study between the samples collected throughout the Hırkadağ Massif, suggesting that the entire massif experienced HT metamorphism. Therefore the regional correlation between the grade of metamorphism and the structural level within the CAM proposed by Gönçüoğlu (1981) and Teklehaïmanot (1993) is not always guaranteed. The reaction rims of cordierite forming around garnet porphyroblasts can be interpreted to reflect decompression from ~7–8 to ~3–4 kbar (and T ~800 °C) (Fig. 6), comparable to published data from similar rocks of the Hırkadağ Massif (Whitney and Dilek, 2001). The LP–HT stage may also coincide with local but widespread granodioritic intrusions likely taking



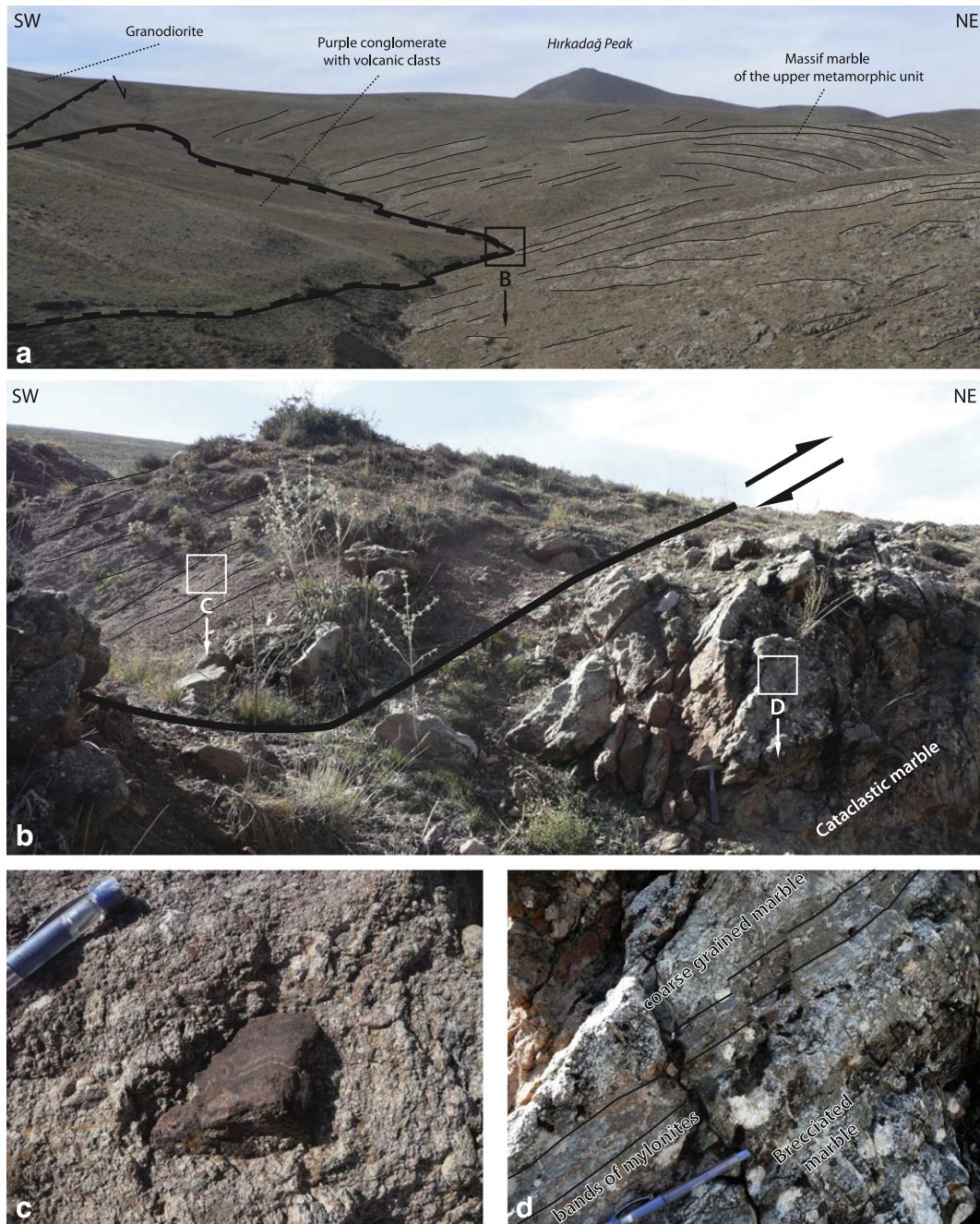


**Fig. 10.** Field structures in the Sığirkalın area: a) panoramic view of Sığirkalın area and structural relationship between massive marble of the upper unit and the overriding purple conglomerate, b) detail of the contact between the marbles and the conglomerates, c) volcanic pebbles in the purple conglomerates, and d) brecciated mylonitic bands from the marble directly below the contact.

place at ~77 Ma (assuming a closure temperature of ~700–660 °C (Scott and St-Onge, 1995)). At this time, deformation was restricted to large-scale open folding without pervasive deformation on the microscale. Note, however, that in the Hırkadağ Massif, there are no further constraints on the process that transported the metamorphic rocks from lower-middle toward upper-crustal depths, reflected by decompression from ~7–8 kbar to ~3–4 kbar.

Along the NE margin of the Hırkadağ Massif, the structurally high massive marbles are cross-cut by (proto-)mylonitic shear bands containing minor muscovite and chlorite, suggesting shearing at low temperature, greenschist facies conditions, consistent with temperature estimates for the activation of shear localization in pure calcite material (de Bresser et al., 2002). At the scale of the massif, the mylonitic shear bands are consistently associated with a normal top-to-the-NE sense

of shear. The  $^{40}\text{Ar}/^{39}\text{Ar}$  ages of  $68.8 \pm 0.9$  Ma for biotite and  $67.0 \pm 1.2$  Ma for K-feldspar from southern metapelites (Lefebvre, 2011) date the cooling of the Hırkadağ Massif below ~325 °C and ~225 °C, respectively, and this cooling may therefore coincide with deformation along the greenschist facies top-to-the-NE mylonites. In the Sığirkalın area, discrete calcite mylonites are overprinted by cataclastic brittle deformation along the same foliation plane, juxtaposing non-metamorphic conglomerates on top of the Hırkadağ high-grade metamorphic and igneous rocks. Within the adjacent Ayhan Basin, similar conglomerates are intercalated with ~72 Ma old volcanics (Advokaat et al., 2014). This implies that the sediments in the hanging wall of the fault were deposited at the surface while the high grade footwall was still at depth corresponding to an ambient temperature of ~400 °C (Fig. 11a). We infer that the Sığirkalın suite of structures represents a top-to-the-NE extensional



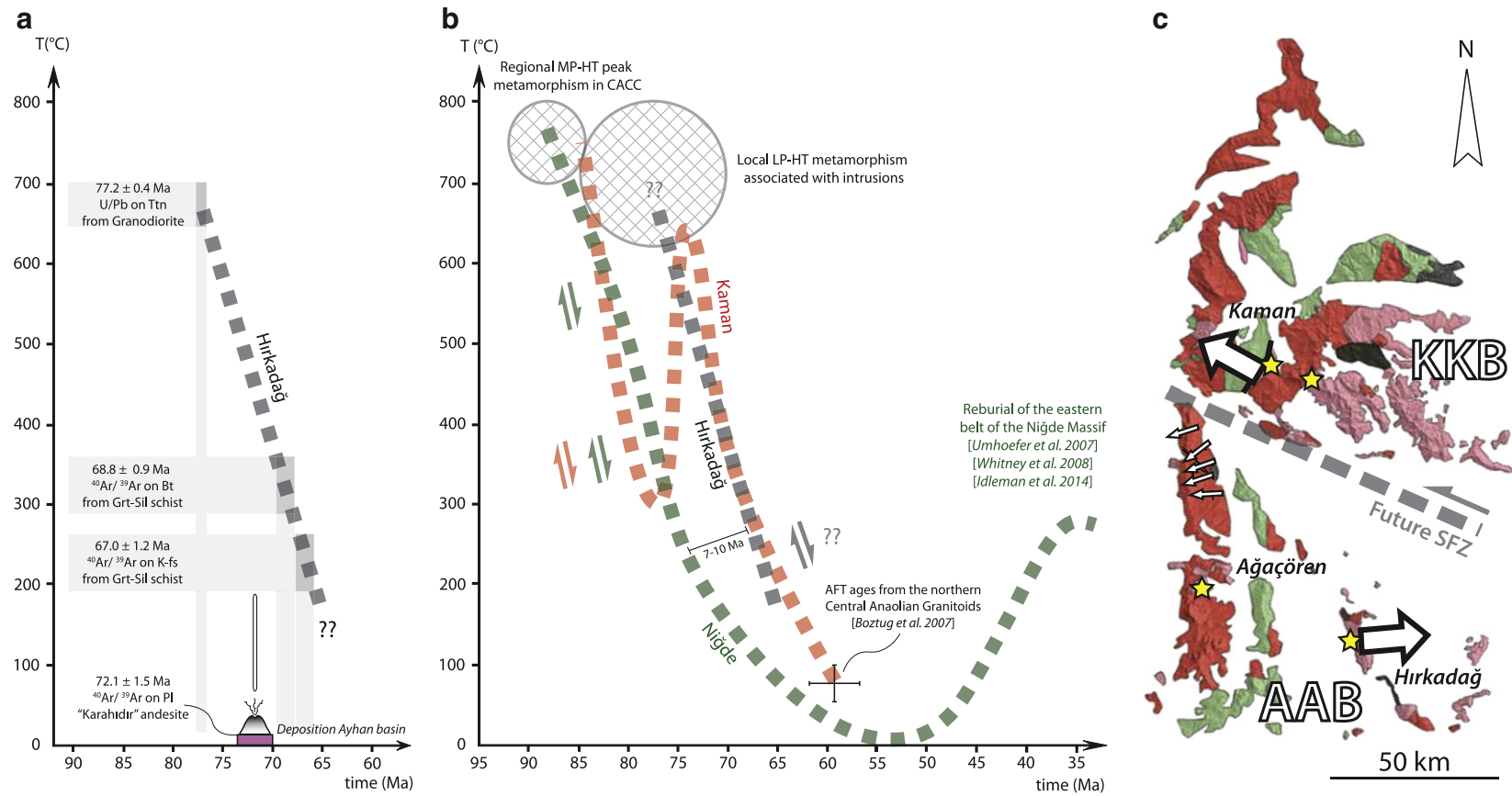


**Fig. 11.** a) Temperature versus age diagram illustrating the cooling trajectory of the Hırkadağ Massif. U/Pb (titanite) and <sup>40</sup>Ar/<sup>39</sup>Ar (biotite and K-feldspar) ages on a granodioritic intrusion (H2699C) and a metapelite rock (H19H) are from Lefebvre (2011). <sup>40</sup>Ar/<sup>39</sup>Ar (plagioclase) age on the "Karahidir" andesite is from Advokaat et al. (2014), b) same diagram as in (a), supplemented with previously published cooling trajectories from other localities in the CACC, i.e., the Niğde Massif (Whitney et al., 2003; Whitney et al., 2007; Gautier et al., 2008; Idleman et al., 2014) and the Kaman area (Köksal et al., 2004; Whitney and Hamilton, 2004; Boztuğ et al., 2009; Lefebvre et al., 2011). Apatite fission track ages from the central Anatolian Intrusives (Boztuğ and Jonckheere, 2007) are also reported. The shearing arrows illustrate when the described detachment structures likely developed during cooling. c) Late Cretaceous restoration of the KKB and AAB based on paleomagnetic data published by Lefebvre et al. (2013). See Fig. 1 for legend. Large arrows represent the restored shear sense along the Kaman and Hırkadağ detachments. Small arrows indicate motion along discrete ductile shear zones from the Ağaçören granitoid reported by Isik (2009). Yellow stars indicate locations LP-HT mineral assemblages reported in Whitney et al. (2001) and this study.

detachment, along which the Hırkadağ basement was exhumed from depths of greenschist facies conditions to the surface. The detachment fault is cross-cut at high-angles by NW–SE trending brittle normal faults that were active during the deposition of the middle part of the Ayhan basin, sometime before the Lutetian (49–41 Ma; Fig. 11a). The Ayhan basin provides evidence for syn-sedimentary normal faulting from the onset of sedimentation ~72 Ma ago, which occurred in a NE–SW extension direction after correction for post-Lutetian compression (Advokaat et al., 2014).

## 5.2. Thermal evolution and exhumation mechanisms of the CACC

The thermal evolution of the Hırkadağ Massif reveals cooling from ~680 to ~225 °C between ~77 and 67 Ma, i.e. a cooling rate of ~45 °C/Ma (Fig. 11a). In Fig. 11b, we compare the obtained temperature–time path for the Hırkadağ Massif with existing data from other metamorphic massifs of the CACC. The cooling rate and age of the Hırkadağ Massif share many similarities with those of the Kaman area after intrusion of the Baranadağ monzonite (Köksal et al., 2004; Boztuğ et al., 2009; Lefebvre et al., 2011). Their thermal evolution shows a consistent cooling pattern of the crystalline rocks at ~30–40 °C/Ma from ~77–75 Ma LP–HT metamorphism to ~60 Ma AFT unroofing age (Fig. 11b) (Boztuğ et al., 2007). By contrast, the cooling histories of the southern Niğde Massif (Whitney et al., 2003; Whitney et al., 2007., Gautier et al., 2008) and the Kaman area prior to the Baranadağ intrusion (Whitney and Hamilton, 2004; Lefebvre et al., 2011) show a higher cooling rate of ~60 °C/Ma from ~700 to ~300 °C, and occurred ~7–10 Ma earlier than in Hırkadağ (Fig. 11b). This difference in rates and ages between the central Anatolian massifs is best explained by immediate cooling after regional MP–HT peak metamorphism (i.e. Niğde and Kaman initial cooling) compared to cooling after local LP–HT metamorphism (i.e. Hırkadağ and Kaman late stage cooling).

In Kaman, the study of calcite microstructures demonstrated that the high-grade metasediments experienced two distinct cooling phases prior and after intrusion of the Baranadağ batholith (Lefebvre et al., 2011). This is a critical piece of information as it suggests that, in this case, the LP–HT overprint described by Whitney et al. (2001) was likely not related to regional isothermal decompression but rather to local effects of later magmatism occurring once the rocks had already cooled down below ~300 °C (Lefebvre et al., 2011). In the Kaman and Hırkadağ areas the cooling trajectories after intrusion are nearly identical and could suggest a comparable scenario where the LP–HT event was associated with local (~75–77 Ma) magmatism. This hypothesis is supported by the presence of a network of pegmatite and aplitic granite dykes and veins throughout the Hırkadağ Massif. At the scale of the CACC, regional MP–HT metamorphism followed by local LP–HT overprint was identified and different P–T paths were reported from four locations: Kaman/Hırkadağ, Akdağ, Niğde and Aksaray/Ağaçören (Figs. 1 and 11c) (Whitney et al., 2001). It is interesting to note that the Akdağ Massif, which contains almost no intrusive rocks, recorded only the regional MP–HT event (5–8 kbar and 550–675 °C (Şahin and Erkan, 1999; Whitney et al., 2001)) while in the Aksaray/Ağaçören area, which is dominated by plutons, only LP–HT metamorphism could be identified (4 kbar, 600–700 °C (Kocak and Leake, 1994; Whitney et al., 2001)). Together with our previous observations from Kaman and Hırkadağ, this suggests a strong correlation between the presence of nearby plutons and identification of LP–HT overprinting assemblages in the CACC (Fig. 11c) which favors the hypothesis involving magmatic heat advection instead of regional isothermal decompression from ~20 to ~10 km.

In the Hırkadağ Massif, the NW–SE trending mineral lineations associated with the regional MP–HT metamorphism are at high angle to the NE–SW stretching lineations from the cross-cutting localized calcite shear-bands related to the newly recognized Hırkadağ detachment. From this, we infer that the extensional detachment was not active during HT metamorphism. This feature, and the suite of marble

microstructures and calcite fabrics of the Hırkadağ detachment, are very similar to the upper crustal extensional detachment identified in the Kırşehir Massif near Kaman (Lefebvre et al., 2011). However, they differ by the nature of their hanging wall: in Kaman, it consists of ophiolitic crustal material, whereas in Hırkadağ the hanging wall is made of the sedimentary rocks from the supradetachment basin. The Hırkadağ detachment exhumed the crystalline rocks to near the surface at the contact with the deeper part of the overlying Ayhan basin, while in Kaman, the detachment was active at ~10 km depth below the CAO and prior to the Baranadağ intrusion (Fig. 11b) (Lefebvre et al., 2011). In this respect, the Hırkadağ detachment should be better compared with the marble detachment or normal fault described in the southern border of the Niğde Massif, separating the CAM from the Paleogene Ulukışla basin (Whitney and Dilek, 1997; Gautier et al., 2002).

In the northern Niğde Massif, the extensional detachment identified by Gautier et al. (2002, 2008) separates high-grade metasediments from ophiolitic gabbros. Below the gabbros, the HT metamorphic deformation occurred along parallel foliations and in the same direction as the younger semi-brittle deformation suggesting that the detachment was active at deeper levels than in Kaman. Therefore, different types or portions of detachment have been recognized in the CACC: (1) the northern Niğde detachment that was rooted at middle or lower crustal levels, (2) the Kaman detachment that exhumed rocks at upper crustal levels, and (3) the Hırkadağ (and possibly southern Niğde) detachments that unroofed rocks from the upper crust to near the Earth surface (Fig. 11b).

## 5.3. Implications for late Cretaceous regional extension and the geodynamic setting of the CACC

Based on paleomagnetic results from the Upper Cretaceous central Anatolian granitoids, Lefebvre et al. (2013) have shown that the CACC was affected by large block rotation and translation during the Paleogene. The Gülşehir–Avanos area is located between the Kırşehir–Kırıkkale block (KKB) in the north, which underwent a slight CCW rotation (~6–9°), and the Ağaçören–Avanos block (AAB) recording ~28–35° CCW rotation. The motion between the two blocks was accommodated by the transpressional Savcıli Fault Zone (SFZ) (Lefebvre et al., 2013). Located south of the north-vergent SFZ, the Hırkadağ and Işıdağı Massifs should belong to the AAB. In Fig. 11c, we restore the position of the KKB and AAB and associated extensional kinematics in their late Cretaceous configuration. Once restored, the ~100 km long “Kırıkkale granitoid belt” and the Ağaçören Intrusive Suite appear continuous and aligned along a ~N–S orientation. Restoring the orientation of the presently top-to-the-NE Hırkadağ detachment and top-to-the-SW discrete ductile shear zones from the Ağaçören granitoid (Isik, 2009) for the ~28–35° counterclockwise vertical axis rotations suggests that Late Cretaceous extension direction was E–W in the AAB (Fig. 11c). On the northern side of the SFZ, the ductile-to-brittle shearing along the Kaman detachment restores to top-to-the WNW in the KKB. This reconstruction implies that the late Cretaceous exhumation of the restored CACC was accommodated by conjugate extensional features such as: top-to-the-WNW detachment (Kaman) and top-to-the-W ductile shear zones (Ağaçören) in the western half of the CACC and top-to-the-E detachment (Hırkadağ) in the east, suggesting a regional E–W directed extension at the scale of the CACC.

As proposed by Lefebvre et al. (2013), this restoration combined with the compositional, temporal and spatial evolution of the CAG, strongly suggests that the CACC evolved above a ~N–S trending, E-dipping subduction zone during the late Cretaceous. In that configuration, the LP–HT conditions of metamorphism associated with widespread magmatism occurring in an extensional tectonic environment are best explained in a context of the development and exhumation of a magmatic arc above an active subduction zone, similar to, for example, the Jurassic magmatic arc in the central Pontides (Okay et al., 2014).

## 6. Conclusions

In order to elucidate the processes associated with the late Cretaceous HT event, the tectonic history of the Hırkadağ Massif has been addressed through an integrated approach involving metamorphic, structural and geochronological analysis. The tectonic history of the Hırkadağ Massif includes a regional MP–HT metamorphic event associated with pervasive top-to-the-SW ductile deformation. The replacement of garnet and sillimanite by cordierite and spinel in metapelitic rocks indicates a LP–HT overprint that may be related to local intrusions. Geochronology on the intrusive granodiorite bodies (likely responsible for the localized granulite facies overprint) yields a titanite U/Pb age of  $77.2 \pm 0.4$  Ma (Lefebvre, 2011). Following the magmatism, the Hırkadağ HT complex cooled down rapidly, reaching  $\sim 325$  °C by  $68.8 \pm 0.9$  Ma and  $\sim 225$  °C by  $67.0 \pm 1.2$  Ma, indicated by  $^{40}\text{Ar}/^{39}\text{Ar}$  cooling ages from biotite and K-feldspar, respectively (Lefebvre, 2011).

Exhumation of the crystalline rocks is documented within the northern marbles by the presence of discrete protomylonitic and mylonitic shear bands having N40–60 stretching lineation directions with a consistent normal top-to-NE sense of shear. The Sığırkalan area exposes the contact associated with this shearing event, between high-grade deformed marbles (with ductile mylonitic shear bands overprinted by cataclases), and late Cretaceous non-metamorphosed conglomerates containing volcanic pebbles. This structure has been interpreted as an upper crustal detachment fault, similar to what has been reported in the NW Kaman area. Regional evaluation of the thermal history of the central Anatolian massifs suggests that the observed local LP–HT metamorphism is most likely associated with thermal effects of nearby plutons instead of being caused by regional decompression. Finally, using the paleomagnetic data of Lefebvre et al. (2013) we restored the Hırkadağ Massif and the CACC to their position prior to rotation and translation of large tectonic blocks. In that configuration, it is clear that the LP–HT metamorphism, magmatism and extensional structures evolved as a result of the development and exhumation of a ~N–S trending magmatic arc experiencing regional E–W extension above an active subduction zone.

## Acknowledgments

This research was financially supported by the Netherlands Research Center for Integrated Solid Earth Sciences, the Netherlands Organization for Scientific Research (NWO) and the DARIUS Programme. Kalijn M. Peters and Philip C. Wehrens acknowledge financial support from the Molengraaff Foundation. The final writing, revision and publication of this work were realizable thanks to the funding by the Continental Dynamics—Central Anatolian Tectonics project, NSF-EAR-1109762. The  $^{40}\text{Ar}/^{39}\text{Ar}$  and U/Pb age dating reported in Côme Lefebvre PhD thesis (mentioned here as Lefebvre (2011)) has been processed by Bart W.H. Hendriks (Geological Survey of Norway, Trondheim) and Fernando Corfu (Department of Geosciences and CEED, University of Oslo) respectively. Tilly Bouten is thanked for her technical support with the microprobe analyses. Osman and Yasin (from *Kirit Pension* in Avanos) are kindly thanked for their logistical support around the study area. The authors are grateful to the three anonymous reviewers who provided helpful comments that significantly improved the manuscript.

## References

Advokaat, E.L., van Hinsbergen, D.J.J., Kaymakci, N., Vissers, R.L.M., Hendriks, B.H.W., 2014. Late Cretaceous extension and Palaeogene rotation-related contraction in Central Anatolia recorded in the Ayhan–Büyüklışla basin. *International Geology Review* 56 (15), 1813–1836.

Akiman, O., Erler, A., Gönçüoğlu, M.C., Güleç, N., Geven, A., Türel, T.K., Kadioğlu, Y.K., 1993. Geochemical characteristics of granitoids along the western margin of the CACC and their tectonic implications. *Geological Journal* 28, 371–382.

Atabey, E., 1989. Kayseri–H19 Paftası Jeoloji Haritası: Ankara. General Directorate of Mineral Research and Exploration (MTA) Publication, Turkey.

Atabey, E., Tarhan, N., Akarsu, B., Taskiran, A., 1987. Serefelikochisar, Panli (Ankara)—Acipinar (Niğde) yöresinin jeolojisi. M.T.A. Report No. 8155, Ankara.

Aydın, N., 1985. Geological evolution of Gümüşkent town and its surrounding in the Middle Anatolian Massif. Communications, de La Faculté des Sciences de l'Université d'Ankara, série C1 Géologie. 31 pp. 43–56.

Bestmann, M., Kunze, K., Matthews, A., 2000. Evolution of a calcite marble shear zone complex on Thassos Island, Greece: microstructural and textural fabrics and their kinematic significance. *Journal of Structural Geology* 22 (11–12), 1789–1807.

Bhattacharya, A., Mazumdar, A.C., Sen, S.K., 1988. Fe–Mg mixing in cordierite: constraints from natural data and implications for cordierite–garnet geothermometry in granulites. *American Mineralogist* 73, 338–344.

Bhattacharya, A., Mohanty, L., Maji, A., Sen, S.K., Raith, M., 1992. Nonideal mixing in the phlogopite–annite binary—constraints from experimental data on Mg–Fe partitioning and a reformulation of the biotite garnet geothermometer. *Contributions to Mineralogy and Petrology* 111 (1), 87–93.

Boztuğ, D., Jonckheere, R.C., 2007. Apatite fission track data from central Anatolian granitoids (Turkey): constraints on Neo-Tethyan closure. *Tectonics* 26 (3).

Boztuğ, D., Tichomirowa, M., Bombach, K., 2007. 207Pb–206Pb single-zircon evaporation ages of some granitoid rocks reveal continent–oceanic island arc collision during the Cretaceous geodynamic evolution of the Central Anatolia, Turkey. *Journal of Asian Earth Sciences* 31, 71–86.

Boztuğ, D., Güney, O., Heizler, M., Jonckheere, R.C., Tichomirowa, M., Otlı, N., 2009. 207Pb–206Pb, 40Ar–39Ar and fission-track geochronology quantifying cooling and exhumation history of the Kaman–Kırşehir Region Intrusions, Central Anatolia, Turkey. *Turkish Journal of Earth Sciences* 18, 85–108.

de Bresser, J.H.P., Evans, B., Renner, J., 2002. On estimating the strength of calcite rocks under natural conditions. *Geological Society of London, Special Publication* 200, 309–329.

de Capitani, C., 1994. Gleichgewichts-phasendiagramme: theorie und software. *European Journal of Mineralogy* 6 (48).

de Capitani, C., Petrakakis, K., 2010. The computation of equilibrium assemblage diagrams with Thriak/Domino software. *American Mineralogist* 95 (7), 1006–1016.

Erkan, E., 1976. Isogrades determined in the regional metamorphic area surrounding Kırşehir and their petrological interpretation (in Turkish with English summary). *Yerbilimleri* 2 (1), 23–54.

Erler, A., Gönçüoğlu, M.C., 1996. Geologic and tectonic setting of the Yozgat Batolith, Northern Central Anatolian Crystalline Complex, Turkey. *International Geology Review* 38, 714–726.

Fayon, A.K., Whitney, D.L., Teyssier, C., Garver, J.I., Dilek, Y., 2001. Effects of plate convergence obliquity on timing and mechanisms of exhumation of a midcrustal terrain, the central Anatolian crystalline complex. *Earth and Planetary Science Letters* 192 (2), 191–205.

Gautier, P., Bozkurt, E., Hallot, E., Dirik, K., 2002. Dating the exhumation of a metamorphic dome: geological evidence for pre-Eocene unroofing of the Niğde Massif (Central Anatolia, Turkey). *Geological Magazine* 139 (5), 559–576.

Gautier, P., Bozkurt, E., Bosse, V., Hallot, E., Dirik, K., 2008. Coeval extensional shearing and lateral underflow during Late Cretaceous core complex development in the Niğde Massif, Central Anatolia, Turkey. *Tectonics* 27 (1).

Genç, Y., Yürür, M.T., 2010. Coeval extension and compression in Late Mesozoic—recent thinned extensional tectonics in central Anatolia, Turkey. *Journal of Structural Geology* 32 (5), 623–640.

Gönçüoğlu-Kuşçu, G., Floyd, P.A., 2002. Geochemical correlations between effusive and explosive silicic volcanics in the Saraykent region (Yozgat), central Anatolia, Turkey. *Geological Journal* 37 (2), 143–165.

Ghent, E.D., Stout, M.Z., 1981. Geobarometry and geothermometry of plagioclase–biotite–garnet–muscovite assemblages. *Contributions to Mineralogy and Petrology* 76, 92–97.

Gönçüoğlu, M.C., 1977. *Geologie des westlichen Niğde Massivs* PhD Thesis Bonn University.

Gönçüoğlu, M.C., 1981. Niğde Masifinde viridin–gnaysin kökeni. *Türkiye Jeoloji Kurumu Bülteni* 24, 45–51.

Gönçüoğlu, M.C., Türel, T.K., 1993. Petrology and Geodynamic interpretation of plagiogranites from Central Anatolian Ophiolites (Aksaray–Turkey). *Turkish Journal of Earth Sciences* 2, 195–203.

Gönçüoğlu, M.C., Türel, T.K., 1994. Alpine collisional-type granitoids from western Central Anatolian Crystalline Complex, Turkey. *Journal of Kocaeli University, Earth Science section* 1, 39–46.

Gönçüoğlu, M.C., Toprak, V., Kuşçu, I., Erler, A., Olgun, E., 1991. Orta Anadolu Masifinin orta bölümünün jeolojisi - bölüm 1: Güney kesim. Turkish Petroleum Corporation (TPAO), Report no. 2909, 140 pp (unpublished).

Gönçüoğlu, M.C., Erler, A., Toprak, V., Olgun, E., Yalıniz, K.M., Kuşçu, I., Köksal, S., Dirik, K., 1993. Orta Anadolu Masifinin orta bölümünün jeolojisi - bölüm 3: Orta Kızılırmak Tersiyer Baseninin jeolojik evrimi. Turkish Petroleum Corporation (TPAO) Report no. 3313, 104 pp (unpublished).

Görür, N., Oktay, F.Y., Seymen, I., Şengör, A.M.C., 1984. Palaeotectonic evolution of the Tuzgölü basin complex, Central Turkey: sedimentary record of a Neo-Tethyan closure. *Geological Society, London, Special Publications* 17 (1), 467–482.

Grove, M., Harrison, T.M., 1996. Ar–40(\*) diffusion in Fe-rich biotite. *American Mineralogist* 81 (7–8), 940–951.

Gülyüz, E., Kaymakci, N., Meijers, M.J.M., van Hinsbergen, D.J.J., Lefebvre, C., Vissers, R.L.M., Hendriks, B.W.H., Peynircioğlu, A.A., 2013. Late Eocene evolution of the Çiçekdağı Basin (central Turkey): syn-sedimentary compression during microcontinent–continent collision in central Anatolia. *Tectonophysics* 602, 286–299. <http://dx.doi.org/10.1016/j.tecto.2012.07.003>.

Harrison, T.M., McDougall, I., 1982. The thermal significance of potassium–feldspar K–Ar ages inferred from Ar–40/Ar–39 age spectrum results. *Geochimica Et Cosmochimica Acta* 46 (10), 1811–1820.



- Holland, T.J.B., Powell, R., 1998. An internally consistent thermodynamic data set for phases of petrological interest. *Journal of Metamorphic Geology* 16 (3), 309–343.
- Idleman, L., Cosca, M.A., Heizler, M.T., Thomson, S.N., Teyssier, C., Whitney, D.L., 2014. Tectonic burial and exhumation cycles tracked by muscovite and K-feldspar 40Ar/39Ar thermochronology in a strike-slip fault zone, central Turkey. *Tectonophysics* 612–613, 134–146.
- İlbeyli, N., Pearce, J.A., Thirlwall, M.F., Mitchell, J.G., 2004. Petrogenesis of collision-related plutonics in Central Anatolia, Turkey. *Lithos* 72, 163–182.
- Isik, V., 2009. The ductile shear zone in granitoid of the Central Anatolian Crystalline Complex, Turkey: implications for the origins of the Tuzgölü basin during the Late Cretaceous extensional deformation. *Journal of Asian Earth Sciences* 34 (4), 507–521.
- Isik, V., Lo, C.-H., Göncüoğlu, M.C., Demirel, S., 2008. 39Ar/40Ar ages from the Yozgat Batholith: preliminary data on the timing of Late Cretaceous extension in the Central Anatolian Crystalline Complex, Turkey. *The Journal of Geology* 116 (5), 510–526.
- Isik, V., Uysal, I.T., Caglayan, A., Seyitoglu, G., 2014. The evolution of intra-plate fault systems in central Turkey: structural evidence and Ar–Ar and Rb–Sr age constraints for the Savcili Fault Zone. *Tectonics* 33. <http://dx.doi.org/10.1002/2014TC003565>.
- Kadioğlu, Y.K., Dilek, Y., Gülec, N., Foland, K.A., 2003. Tectonomagmatic evolution of bimodal plutons in the central Anatolian crystalline complex, Turkey. *Journal of Geology* 111 (6), 671–690.
- Kaymakci, N., Özçelik, Y., White, S.H., van Dijk, P.M., 2009. Tectono-stratigraphy of the Çankiri Basin: late Cretaceous to early Miocene evolution of the Neotethyan suture zone in Turkey. *Collision and Collapse at the Africa–Arabia–Eurasia Subduction Zone*. Geological Society of London Special Publication 311, pp. 67–106.
- Ketin, I., 1966. Tectonic units of Anatolia (Asia Minor). *Mineral Research and Exploration Bulletin* 66, 23–34.
- Kocak, K., Leake, B.E., 1994. The petrology of the Ortaköy District and its ophiolite at the western edge of the middle Anatolian Massif, Turkey. *Journal of African Earth Sciences* 18 (2), 163–174.
- Köksal, S., Göncüoğlu, M.C., 1997. Geology of the İdiş Dağı–Avanos area (Nevşehir–Central Anatolia). *Mineral Research and Exploration Bulletin* 119, 41–58.
- Köksal, S., Göncüoğlu, M.C., Floyd, P.A., 2001. Extrusive members of post-collisional A-type magmatism in Central Anatolia: Karahadır volcanics, İdiş Dağı–Avanos, Turkey. *International Geology Review* 43, 683–694.
- Köksal, S., Romer, R.L., Göncüoğlu, M.C., Toksoy-Köksal, F., 2004. Timing of post-collisional H-type to A-type granitic magmatism: U–Pb titanite ages from the Alpine central Anatolian granitoids (Turkey). *International Journal of Earth Sciences* 93, 974–989.
- Kuşçu, G., Floyd, P.A., 1995. Petrography and geochemistry of dacites and rhyodacites from Saraykent Region, Yozgat, central Anatolia, Turkey. *International Earth Science Colloquium on the Aegean Region (IESCA 1995) Abstracts*, 37.
- Lefebvre, C., 2011. The Tectonics of the Central Anatolian Crystalline Complex: A Structural, Metamorphic and Paleomagnetic Study PhD thesis, Utrecht Studies in Earth Sciences vol. 3. Departement Aardwetenschappen (147 p. (available and downloadable <http://dspace.library.uu.nl/handle/1874/214266>)).
- Lefebvre, C., 2015. Comment on “Late Cretaceous extension and Palaeogene rotation-related contraction in Central Anatolia recorded in the Ayhan–Büyükkışla basin” by Advokaat et al. 2014. *International Geology Review* 57 (13), 1707–1711. <http://dx.doi.org/10.1080/00206814.2015.1025242>.
- Lefebvre, C., Barnhoorn, A., van Hinsbergen, D.J.J., Kaymakci, N., Vissers, R.L.M., 2011. Late Cretaceous extensional denudation along a marble detachment fault zone in the Kırşehir Massif near Kaman, Central Turkey. *Journal of Structural Geology* 33 (8), 1220–1236. <http://dx.doi.org/10.1016/j.jsg.2011.06.002>.
- Lefebvre, C., Barnhoorn, A., van Hinsbergen, D.J.J., Kaymakci, N., Vissers, R.L.M., 2012. Reply to Genç and Yürür’s comments on: “Late Cretaceous extensional denudation along a marble detachment fault zone in the Kırşehir massif near Kaman, Central Turkey”. *Journal of Structural Geology* 36, 90–93. <http://dx.doi.org/10.1016/j.jsg.2011.12.005>.
- Lefebvre, C., Meijers, M.J.M., Kaymakci, N., Peynircioğlu, A.A., Langereis, C.G., van Hinsbergen, D.J.J., 2013. Reconstructing the geometry of central Anatolia during the late Cretaceous: large-scale Cenozoic rotations and deformation between the Pontides and Taurides. *Earth and Planetary Science Letters* 366, 83–98. <http://dx.doi.org/10.1016/j.epsl.2013.01.003>.
- MacKenzie, W.S., Adams, A.E., 2003. *A Colour Atlas of Rocks and Minerals in Thin Section*. Manson Publishing Ltd, London.
- McDougall, I., Harrison, T.M., 1999. *Geochronology and Thermochronology by the 40Ar/39Ar Method* (2nd edition). Oxford Univ. Press, New York, p. 269.
- Mckenna, L.W., Hodges, K.V., 1988. Accuracy versus precision in locating reaction boundaries—implications for the garnet plagioclase aluminum silicate quartz geobarometer. *American Mineralogist* 73 (9–10), 1205–1208.
- Meijers, M.J.M., Kaymakci, N., van Hinsbergen, D.J.J., Langereis, C.G., Stephenson, R.A., Hippolyte, J.C., 2010. Late Cretaceous to Paleocene oroclinal bending in the central Pontides (Turkey). *Tectonics* 29.
- Okay, A.I., Tüysüz, O., 1999. Tethyan sutures of northern Turkey. In: Durand, B., Jolivet, L., Horváth, F., Séranne, M. (Eds.), *The Mediterranean Basins: Tertiary Extension within the Alpine Orogen*. Geol. Soc. London Spec. Publ. 156, pp. 475–515.
- Okay, A.I., Sunal, G., Tüysüz, O., Sherlock, S., Keskin, M., Kylander-Clark, A.R.C., 2014. Low-pressure–high-temperature metamorphism during extension in a Jurassic magmatic arc, Central Pontides, Turkey. *Journal of Metamorphic Geology* 32, 49–69.
- Oktay, F.Y., 1981. Stratigraphy and Geological Evolution of the Sedimentary Cover of the Central Anatolian Massif in the Kaman–Kırşehir Region: Turkish Geological Society, 35th Scientific and Technical Assembly, Symposium on the Geology of Central Anatolia.
- Şahin, M.B., Erkan, Y., 1999. The index minerals and mineral assemblages determined in metamorphites of Evciler–Çatköy (Çayralan–Yozgat) segment of the Akdağmadeni Massif. *Mineral Research and Exploration Bulletin* 121 (83–100).
- Scott, D.J., St-Onge, M.R., 1995. Constraints on Pb closure temperature in titanite based on rocks from the Ungava orogen, Canada: implications for U–Pb geochronology and P–T–t path determinations. *Geology* 23 (12), 1123–1126.
- Şengör, A.M.C., Yılmaz, Y., 1981. Tethyan evolution of Turkey—a plate tectonic approach. *Tectonophysics* 75 (3–4), 181–241.
- Seymen, I., 1981. Stratigraphy and metamorphism of the Kırşehir Massif around Kaman (Kırşehir–Turkey). *Mineral Research and Exploration Bulletin* 24, 7–14.
- Seymen, I., 1982. Kaman Dolayında Kırşehir masifi’nin Jeolojisi. İTÜ Maden Fakültesi, Doçentlik Tezi, İstanbul (164 p.).
- Seymen, I., 1984. Geological evolution of the metamorphic rocks in the Kırşehir Massif. *Ketin Sempozyumu* 133–148.
- Spear, F.S., 1993. *Metamorphic Phase Equilibria and Pressure–Temperature–Time Paths*. Monograph 1. Mineralogical Society of America, Chantilly, Virginia.
- Spear, F., Cheney, J., 1989. A petrogenetic grid for pelitic schists in the system SiO<sub>2</sub>–Al<sub>2</sub>O<sub>3</sub>–FeO–MgO–K<sub>2</sub>O–H<sub>2</sub>O. *Contributions to Mineralogy and Petrology* 101 (2), 149–164.
- Teklehaïmanot, L.T., 1993. Geology and petrography of Gülşehir area, Nevşehir, Turkey. MSc Thesis, Middle East Technical University, Ankara, Turkey [unpublished].
- Toprak, V., 1994. Central Kızılırmak Fault Zone: northern margin of Central Anatolian Volcanics. *Turkish Journal of Earth Sciences* 3, 29–38.
- Umhoefer, P.J., Whitney, D.L., Teyssier, C., Fayon, A.K., Casale, G., Heizler, M.J., 2007. Yo-yo tectonics in a wrench zone. In: Till, A.B., et al. (Eds.), *Exhumation associated with continental strike-slip systems*. Geological Society of America Special Paper 434, pp. 35–57.
- Vache, R., 1963. Akdağmadeni kontak yatakları ve bunların Orta Anadolu Kristalinine karşı olan jeolojik çerçevesi (in Turkish with English Abstract). *Bulletin. Mineral Research and Exploration Institute (Turkey)* 60, 20–34.
- Whitney, D.L., Dilek, Y., 1997. Core complex development in central Anatolia. *Geology* 25, 1023–1026.
- Whitney, D.L., Dilek, Y., 1998. Metamorphism during Alpine crustal thickening and extension in central Anatolia, Turkey: the Niğde metamorphic core complex. *Journal of Petrology* 39 (7), 1385–1403.
- Whitney, D.L., Dilek, Y., 2001. Metamorphic and tectonic evolution of the Hırkdağ Block, Central Anatolian Crystalline Complex. *Turkish Journal of Earth Sciences* 10, 1–15.
- Whitney, D.L., Evans, B.W., 2010. Abbreviations for names of rock-forming minerals. *American Mineralogist* 95 (1), 185–187.
- Whitney, D.L., Hamilton, M.A., 2004. Timing of high-grade metamorphism in central Turkey and the assembly of Anatolia. *Journal of the Geological Society* 161, 823–828.
- Whitney, D.L., Teyssier, C., Dilek, Y., Fayon, A.K., 2001. Metamorphism of the Central Anatolian Crystalline Complex, Turkey: influence of orogen-normal collision vs. wrench-dominated tectonics on P–T–t paths. *Journal of Metamorphic Geology* 19 (4), 411–432.
- Whitney, D.L., Teyssier, C., Fayon, A.K., Hamilton, M.A., Heizler, M., 2003. Tectonic controls on metamorphism, partial melting, and intrusion: timing and duration of regional metamorphism and magmatism in the Niğde Massif, Turkey. *Tectonophysics* 376 (1–2), 37–60.
- Whitney, D.L., Teyssier, C., Heizler, M.T., 2007. Gneiss domes, metamorphic core complexes, and wrench zones: thermal and structural evolution of the Niğde massif, central Anatolia. *Tectonics* 26, TC5002.
- Yaliniz, M.K., 2008. A geochemical attempt to distinguish forearc and back Arc ophiolites from the “supra-subduction” central Anatolian ophiolites (Turkey) by comparison with modern oceanic analogues. *Ophioliti* 33 (2), 119–134.
- Yaliniz, K.M., Göncüoğlu, M.C., 1998. General geological characteristics and distribution of the Central Anatolian Ophiolites. *Yerbilimleri* 20, 19–30.